FACULTY OF SCIENCE
UNIVERSITY OF COPENHAGEN

Heat Profiling of Optically Trapped Gold Nanoparticles using Vesicle Release

Anders Kyrsting

Supervisor: Lene B. Oddershede

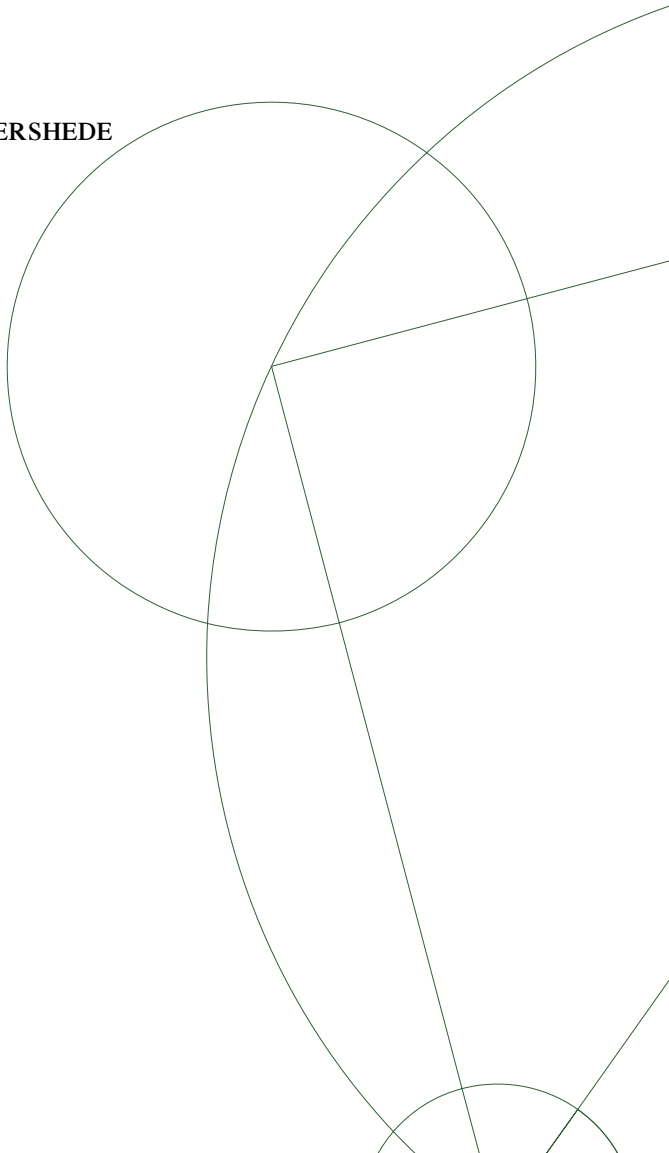

A Thesis Presented for the Degree of
Cand. Scient. in Physics

Niels Bohr Institute
University of Copenhagen
Denmark

August 3, 2010

Abstract

The purpose of this speciale-thesis is to accurate measure the heating from optically trapped gold nanoparticles with diameters 60, 80, 100, 150, and 200 nm. Optical tweezers operating at a wavelength of 1064 nm are used to both control the particles position and confer irradiation, which is absorbed by the gold particles. The temperature profile is then measured by letting $DC_{15}PC$ phospholipid vesicles approach the trapped gold particle. At a critical distance between vesicle and gold particle, the heat at the vesicle exceeds the lipid phase transition temperature, which causes a transient porosity of the lipid vesicle. This porosity can be detected because the fluorophores inside the vesicle leak out. By knowing the phase transition temperature for the lipids, the surface temperature of the gold particles can be inferred through the Goldenberg relation. For 60, 80, and 100 nm the temperature increase lies within 371-523^{o}K/W, while for 150 and 200 nm it is between 242-254^{o}K/W. The increase in scattering cross section, compared to the polarizability, with gold particle size is proposed to cause an axial displacement in the trap, which in turn affects the irradiance for a given size of particle. This is able to account for the difference in temperature increase for each gold particle size.

Acknowledgements

This work has been carried out at the optical tweezers group at NBI, where I was made to feel very welcome by the entire group. In particular I would like to thank my supervisor Lene Oddershede for her great support and advice during the last year, and Poul Martin Bendix for helping me to get started on the project and being invaluable in the lab.

At the c-room I had the fortune to meet many new friends and I would like to thank them all for their uplifting company A thanks go out to Pia, Ninna, Natascha, and Katrine for their comments and proof-reading assistance.

Finally, I very much appreciate the support by my family through the final year of my study. Sara was always the light I turned to - for which I am ever grateful.

Table of Contents

Chapter 1

Introduction

Gold nanoparticles exhibit a strong absorption of light over a wide range of wavelengths, this is despite their tiny sizes of only a few nanometers to about 250 nm. This absorption of energy is converted to heat inside the particles by a photo-thermal process. Given a sufficiently high amount of light on a particle, it will then heat up and transfer its heat into the vicinity. This increase in temperature is highly localized around the gold particle, with a halving of the temperature induced just a particle radius away.

Many research groups have demonstrated possible uses for gold particles. Of these, most have exploited heating by keeping the irradiance of light at the maximum absorbance wavelength for the particles, which lies in the middle of the visual spectrum. It is possible to use the heat development to kill off cancer tumors[1, 2], using either passive or direct targeting of tumors as seen in figure 1.1.

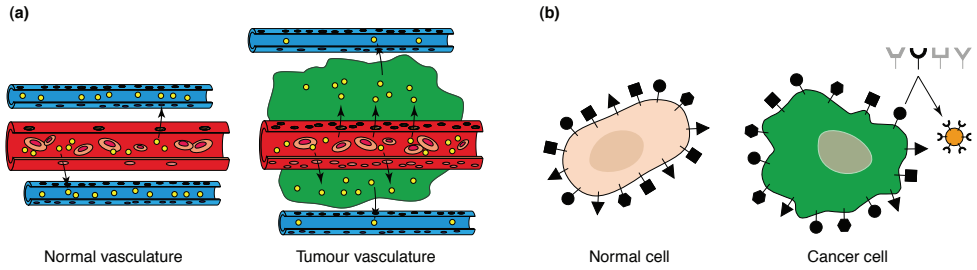

Figure 1.1: Passive and targeted medicinal therapies. a) The higher retention of fluids near cancerous tumors, passively accumulates more gold particles than healthy tissues. b) Direct targeting of tumors by the use of anti-body tagged gold particles. Original figure by Pissuwan[1].

It has also been shown possible to use artificial bio-membrane vesicles as cargo vessels[3], carrying drugs for a local delivery. These cargo vesicles also incorporate gold particles, so that the drugs inside can be released on rupture of the cargo carriers by induced

heat from the gold particles. These biological applications are enticing and practically realizable, as it has been shown that gold particles are not toxic to cells[4].

Heating by gold particles may also prove important to other fields, such as in creating patterns in substrates by processing the material with a single gold particle[5].

For the biological applications it seems more feasible to employ near infrared illumination of gold particles, as in general bio-samples have a minimum of absorption in this range - important for avoiding collateral damage. However, to effectively utilize gold particles as a variable and local heating mechanism, it is first needed to accurately characterize the temperature which develops during irradiance.

This thesis will be concerned with the determination of surface temperature for these gold particles at a given intensity for the near-IR wavelength of 1064 nm. Optical tweezers will be used to both maintain a stable position of the particles, and to quantify the light absorbed by the gold particles when held in the tweezers. The temperature increase will then be measured at a distance from the particle, by using the permeability of lipid bilayers at their phase transition temperature. Permeability of lipid vesicles can be directly detected as the fluorescent cargo inside leaks out, visualized by imaging with confocal fluorescent microscopy. This experimental scheme is illustrated in figure 1.2.

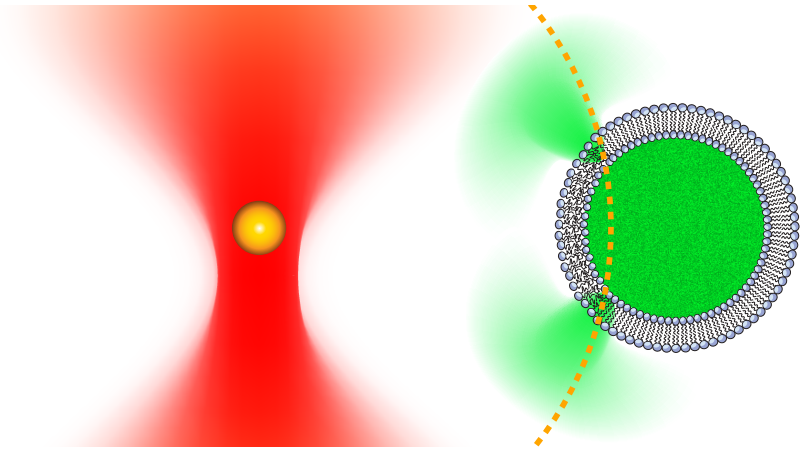

Figure 1.2: An optically trapped gold particle creates a temperature at a distance of the orange line, which exactly causes a permeability in the vesicle, letting the fluorescent dye inside leak to the outside.

1.1 Outline

The thesis contains three general parts for which the structure is as follows.

First, the theoretical basis for the scattering and absorption of gold particles is presented in chapter 2. These are directly related to the forces which an optical trap may exert on the gold particles, as shown in chapter 3. Lipid bilayers and their inherent ability to function as temperature probes are examined in chapter 4.

Second, the design and methodology of the experimental work are detailed in chapter 5. Here the workbench setup for the collection of possible phenomena is shown and discussed.The analysis of data and the following results is put forward in chapter 6, followed by a general discussion ,and finally the conclusion in chapter 7. The relevant appendices are presented after this.

Immediately after the appendix, a pre-print of a soon to be submitted article is attached. This article is based entirely on the work presented in this thesis.

Chapter 2

Mie theory

In order to attain theoretic expectations for the experimental results, a model is needed that quantifies how strongly the gold nanoparticles absorb light and therefore heat up when exposed to incoming radiation.

This chapter will introduce a theoretic solution based on Maxwell's equations for the scattering and absorption of light by gold nanoparticles.

The concept of optical cross section will appear in this chapter and is defined as the amount of light scattered or absorbed by an object, compared to the incoming light irradiance - or watts per area.

2.1 Solution for propagating EM wave scattering on a sphere

Around year 1900 both the German physicist Gustav Mie and the Danish physicist Ludvig Lorenz were concerned with finding a solution by Maxwell's equations to the propagation of EM plane waves in and around sub-micrometer dielectric particles. For the most part, Mie is credited with the discovery. While Lorenz's solution is very similar, it was Mie's that was picked up by Stratton in 1941 [6] and reformed in a briefer mathematical envelope, something which can not be ascribed to the original work. A good read with excellent comments can be found in Bohren & Huffman (1983)[7], who employ a clear writing style with sufficient detail to be self-contained.

Mie found that in the simplest case of a sphere as illustrated in figure 2.1, the interaction of a plane wave with the object could be described entirely analytically - although the method required the sum of all the partial orthogonal Bessel functions to complete the wave. The number of partial waves necessary for reaching precision on a convergent value in the solution depends on the size-ratio of sphere to wavelength, so for finding the actual relevant value, be it scattering or absorption, the calculation workload increases rapidly with increasing size for the same numerical precision. The general interest for

this type of solution is that many particles have spherical or spheroid shape, as is indeed the case for the gold nanoparticles.

Figure 2.1: Illustration of the problem considered by Mie: A plane electro-magnetic wave interaction with a sphere, embedded in a medium of different refractive and extinction optical properties than the sphere itself.

If a given dielectric sphere contains free electrons, we will need to consider the average collision distance for the free electrons if it is comparable to the size of the particle. This could mean that internal surface-scattering may be a major contributor to the overall behavior of the particle electron density to an external field. Fortunately, this effect is mainly of importance in sub 10 nm sized particles[8]. For the size range considered in this thesis the bulk optical constants are applicable, as both the pure number of atoms involved implying bulk characteristics - as well that the mean free path for electrons is not inhibited to any large degree.

2.1.1 Mie solution coefficients

While the complete Mie solution is intriguing in its elegance, only the main results will be highlighted here for the sake of brevity.

Given a traveling linearly polarized plane wave, it is possible to express the wave and the sphere surface in spherical polar coordinates, with respect to the center of the sphere. By introducing spherical Bessel functions known as Riccati-Bessel functions, the gain in shorthand notation later is significant:

ψ_n is defined on Bessel functions of the first kind ($J_n(z)$) as

$$\psi_n(z) = \sqrt{\frac{\pi z}{2}} J_{n+1/2}(z) \quad , \tag{2.1}$$

and ξ_n is defined on Bessel functions of the second kind ($N_n(z)$):

$$\xi_n(z) = -\sqrt{\frac{\pi z}{2}} N_{n+1/2}(z) \quad . \tag{2.2}$$

Here the n indicates the order of the Bessel functions, while z is the complex argument. Then by expanding the wave in an analytical exact multipole of these Bessel functions,

the scattered- and absorbed wave quantities can be determined from the bulk optical constants of refraction and extinction, which are included in the definition of the complex refractive index:

$$N = n_{\text{ref}} + ik_{\text{ext}} \quad , \tag{2.3}$$

where n_{ref} is the normal refractive index and k_{ext} is the extinction coefficient. Here m will be the complex refractive index of the sphere with respect to the medium.

By setting the sphere-medium interface in refractive index at the sphere radius, a set of linear equations is found as a solution. The set has a number of coefficients to be determined numerically to give the scattered and absorbed wave amplitudes. Following the notation given in Kreibig[9] under the assumption that the permeability of the medium and sphere is equal, the solution coefficients to be calculated for the scattered field are given as

$$a_n = \frac{m\psi_n(mx)\psi_n'(x) - \psi_n'(mx)\psi_n(x)}{m\psi_n(mx)\xi_n'(x) - \psi_n'(mx)\xi_n(x)} \quad , \tag{2.4}$$

$$b_n = \frac{\psi_n(mx)\psi_n'(x) - m\psi_n'(mx)\psi_n(x)}{\psi_n(mx)\xi_n'(x) - m\psi_n'(mx)\xi_n(x)} \quad . \tag{2.5}$$

Here x is the size-parameter as $x = kr$, with k being the wave vector in the medium, and r the sphere radius. Mark indicates the first derivative to the entity in parentheses.

This is a very compact representation but for simplicity of programming, spherical Bessel functions are used in the determination as described in detail in appendix 8.1.1.

The n modes from equations 2.4 and 2.5 are shown in figure 2.2, through a visualization of these Mie coefficients. Here the EM-field at a distance from the sphere is illustrated, corresponding to the increasing complexity when considering higher n coefficients. Ideally all modes should be summed up to give the exact coefficient; but the contribution of higher modes falls off fast, so a fair precision can be reached by only including a few of these partial waves. Here, the highest order applied is given by the closest integer of $n_{\max} = x + 4x^{1/3} + 2$ as suggested by Wiscombe[10].

Returning to physical observables, the relevant properties can now be found by insertion of the solution coefficients and integration over the sphere, yielding the optical cross sections for extinction and scattering:

$$C_{\text{ext}} = \frac{2\pi}{k^2} \sum_{n=1}^{\infty} (2n+1)(|a_n|^2 + |b_n|^2) \quad , \tag{2.6}$$

and

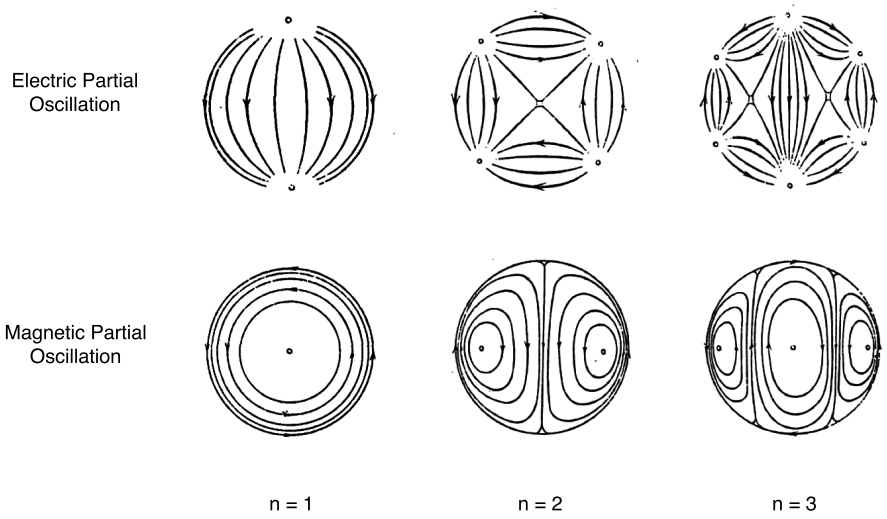

Figure 2.2: Electric far field of the modes corresponding to the n'th wave-component as used in equations 2.4, 2.5. The first mode is a dipole, the second a quadrupole, etc. Adapted from [11]. By superposition of higher order modes the model approaches the Maxwell field description, with additional terms n needed as the size factor x increases to maintain the same accuracy.

$$C_{\text{sca}} = \frac{2\pi}{k^2} \sum_{n=1}^{\infty} (2n+1) Re\{a_n + b_n\} \quad . \tag{2.7}$$

The absorption in the sphere is now given by the definition: $C_{\text{abs}} = C_{\text{ext}} - C_{\text{sca}}$.

These values are only functions of the complex refractive index m, the size parameter x, and the incoming plane EM field as given by k. It should be noted that the bulk material optical properties of refraction and reflection vary with wavelength and therefore the values of the k-dependent refractive index are constructed from the values in the literature[12, 13]. These are then interpolated in wavelength, to give a higher resolution of optical spectra as performed in the next section. The viability of this method is shown in figure 2.3, where the interpolated data is seen as smooth between original literature values.

2.1.2 Theoretical characteristics of gold spheres

The Mie solution for extinction, scattering, and absorption for a 100 nm gold sphere is strongly dependent on the wavelength of the incoming light, as seen in figure 2.4. The calculated values are represented relative to the geometric cross section of the spherical particle by

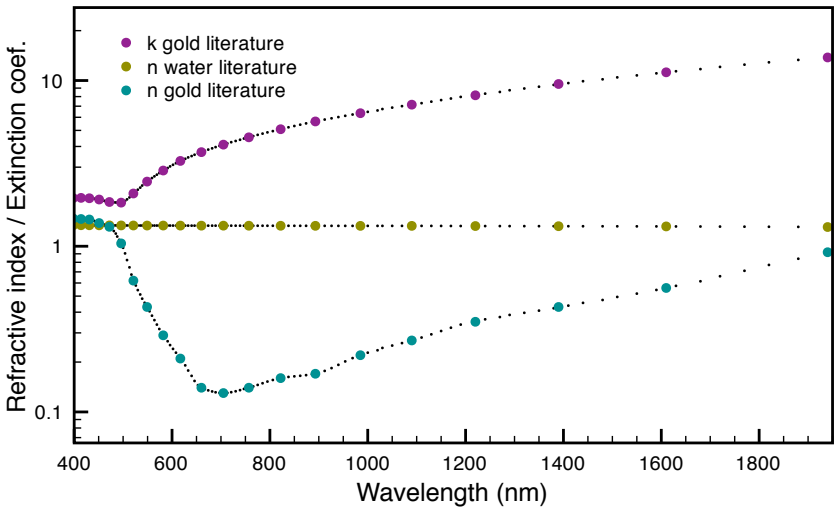

Figure 2.3: Interpolation of refractive and extinction coefficients for gold and water. Large dots represent the data available in literature and the smaller dots show the interpolated data.

$$Q_{\text{ext/sca/abs}} = \frac{C_{\text{ext/sca/abs}}}{\pi r^2} \quad . \tag{2.8}$$

Absorption and scattering are comparable in magnitude for the sphere up till the main resonant frequency at around 550 nm; after which the scattering is the major interaction mode with absorption rolling off fast. For very dilute solutions of gold particles, the experimentally found spectra show a very close relationship with the Mie theory[8, 14]. The main feature for 100 nm gold particles and below is the strong peak, which red-shifts slightly with size. This explains the strong red coloring of solute gold particles, which does exhibit strong red color - absorption is high for blue light, with intense scattering of red light. For sizes above 100 nm there is a gradual shift into a more red/brown color tone, as seen in figure 2.9.

By comparing the spectrum predicted for a 100 nm gold particle to a spectrum mentioned in literature[15], there is a very good agreement to the physical phenomena as seen in figure 2.5. That the Maxwellian solution fits well with actual spectra validates the use of calculated cross sections. Synthesis of gold particles results in nearly spherical beads[16], but the crystal structure and its growth limit the quality of the spherical model assumption. The deviation from physical values at wavelength of 350-500 nm may be attributed to the induced higher order oscillations, which are considerable more complex compared to the dipole.

For an increase in particle size, the energy required to induce a dipole is lower, so the first

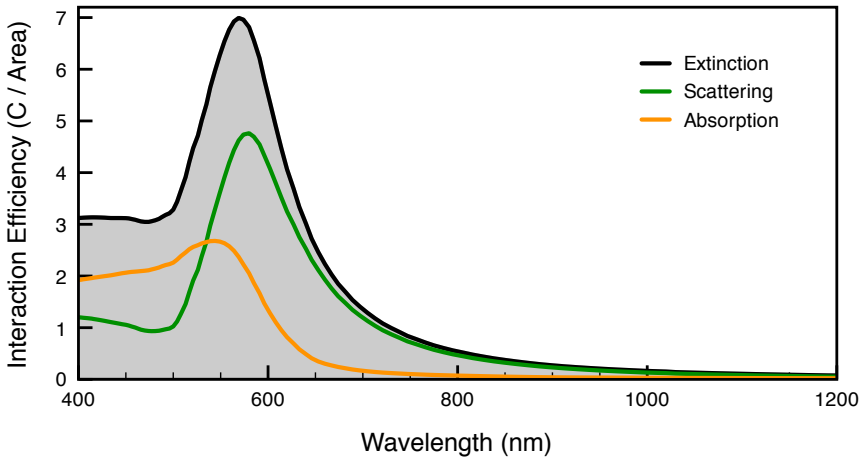

Figure 2.4: Optical properties for a 100 nm gold particle, as calculated by Mie's solution and normalized by the physical cross section of the sphere. The extinction is the sum of contributions from both scattering and absorption by the sphere.

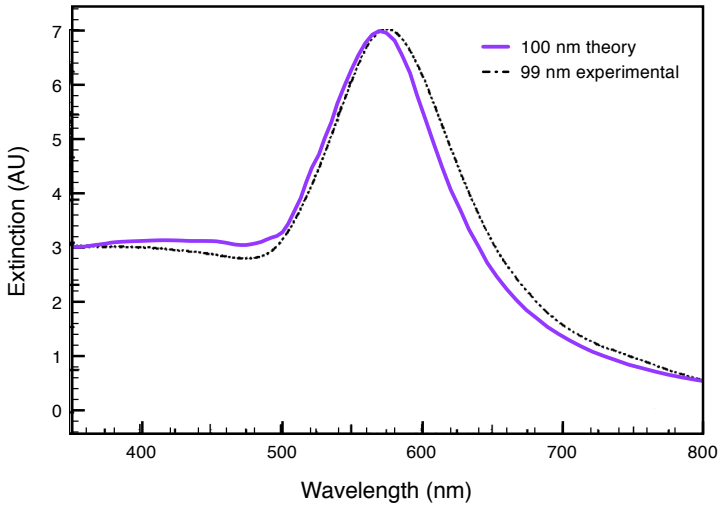

Figure 2.5: Comparing Mie theory to experimental optical spectrum in the light range 350-800 nm. The figure contain data from Link[15] for 99 nm gold particles in water, seen as the black dotted line. A calculated spectrum using the Mie solution is seen as the solid purple line for the size of 100 nm.

term in the Mie solution is shifted to a longer wavelength. Additionally, the amplitudes of higher order modes are increased as seen for a 200 nm gold particle in figure 2.6, where there is a marked difference in the optical spectrum compared to that of the 100 nm particle in figure 2.4. While the absorption is still quite small for the larger particle at the 1064 nm wavelength of the optical trapping laser, the scattering is much higher - a quality which will be detailed in chapter 6.

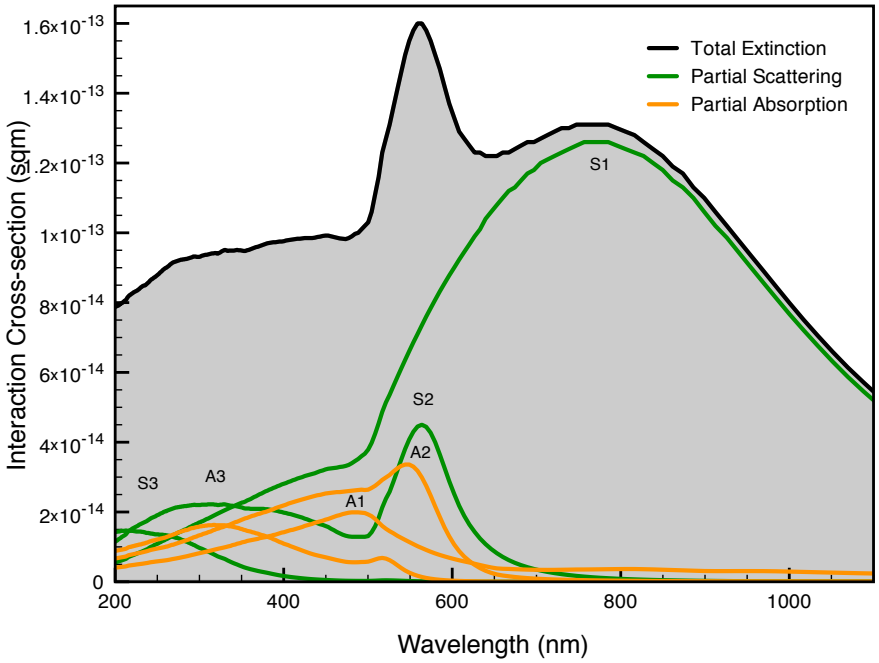

Figure 2.6: Detailed individual scattering and absorption modes for a 200 nm gold particle from equations 2.6 and 2.7. The scattering contributions are seen as Sn with n indicating the Mie coefficient order - likewise for the absorption: An. The total extinction spectrum is a sum of the individual multi-pole elements. S1 and A1 are the scattering and absorption dipole interaction parts, as illustrated in figure 2.2 with n = 1, etc.

To gain insight into how the respective interaction efficiencies scale with different photonic energies and particle sizes, the Mie solution was applied to cover this parameter-space. This may allow arguments regarding the scattering of optically trapped gold particles, based on the interaction strength of the trap and particle. The extinction is seen in figure 2.7, as normalized to the physical cross section (πr^2) at a given radius. There is relatively weak interaction until the particles reach a size of about 40 nm in radius, with periodicity in the oscillating maxima at every 50 nm in radius - starting at for example 550 nm wavelength. Each maxima is a new order mode in the Mie equations, with the first a dipole, then quadrupole, etc.

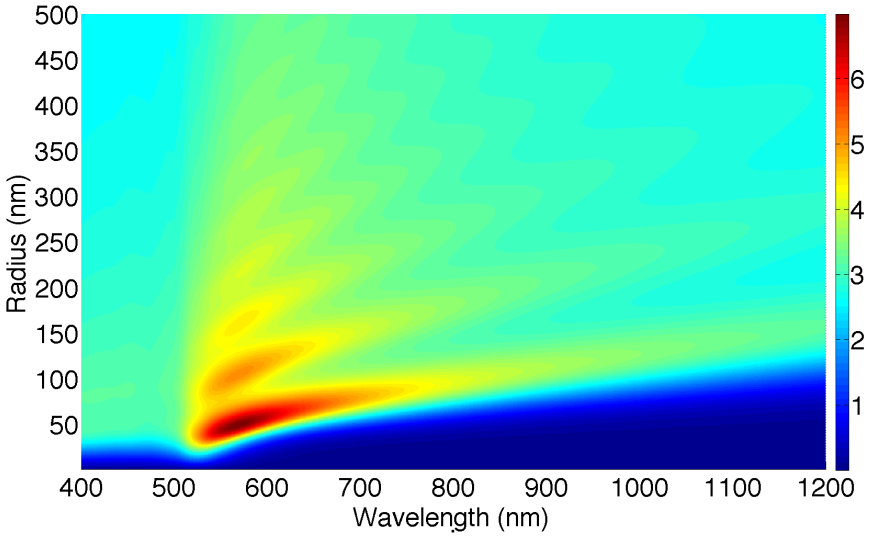

Figure 2.7: Extinction efficiency, see equation 2.8, for 2-1000 nm gold particles. The color bar shows Q_{ext}. There is a marked periodicity in extinction efficiency; for example with increasing radius for 550 nm light, the peaks are displaced approximately with every 50 nm increase in radius.

Focusing on the interaction at the trapping laser wavelength, it is seen in figure 2.8 that the scattering and absorption are linear on a log-log plot up to a radius of 100 nm. While this is not the case for all other wavelengths or size ranges, it is elegant and a result of the strong dipole interaction at low photon energies. At radii above 30 nm, scattering becomes the major interaction for the particles at the 1064 nm wavelength. Above a radius of 100 nm, the influence from higher order modes starts to set in.

2.2 Summary

This chapter illustrates the robustness of the Mie theory, which allows a prediction of extinction, scattering, and absorption of the gold particles during interaction with the trapping laser. A certain limitation is the focused Gaussian beam profile of the 1064 nm laser, but using the properties derived for a plane-wave should transfer well to the scattering quantities of the gold particles taking place near the focus of the optical trap.

Having now determined a theoretical absorption coupling of light to particle, it is possible to include this in a model for the heating of gold particle as performed in the results chapter 6. Mie results can also be employed to determine forces for optical tweezers, as will be shown in chapter 3.

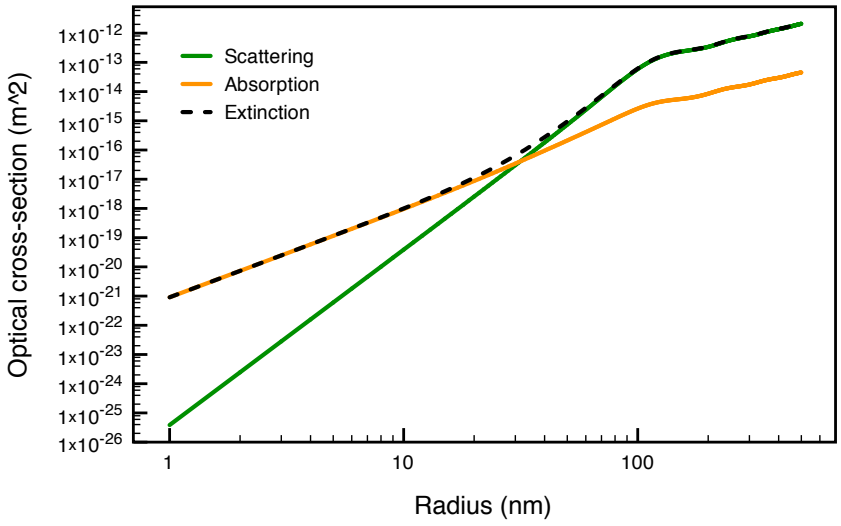

Figure 2.8: Optical cross sections at 1064 nm for 2-1000 nm gold particles. Note the shift with size from almost pure absorption to near only scattering.

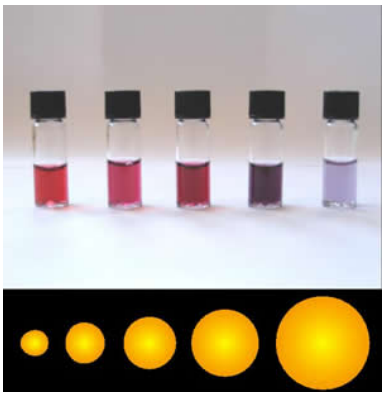

Figure 2.9: Color shifting of gold particles from red to brown with increasing size, figure by [17].

Chapter 3

Optical tweezers

Optical tweezers allow a high degree of maneuverability and offer a good estimation of the irradiation of trapped gold nanoparticles. By the combination of these two elements, it is the technique of choice for characterizing the gold particles in a controlled fashion.

The optical basis and history of the method will here be examined in brief. This will be followed by an overview of the forces that are possible to exert on trapped particles according to models. The motion of trapped particles can be used to record forces applied during experiments by comparing the position data to the expected thermal motion, as will be clarified towards the end of this chapter.

3.1 Bead in a focused Gaussian beam

In 1970, Ashkin[18] found that it was possible to accelerate micron-sized latex spheres by a combination of scattering- and refraction pressure imparted by a focused Gaussian laser beam. Elastic scattering and refraction of photons on an object apply force to the object in accordance with Newton's third law. This force is derived from the momentum of light as based on the energy of its quantum, with the energy found by de Broglie as

$$\mathbf{p} = \frac{\mathbf{E}}{c} = \hbar\mathbf{k} \quad , \tag{3.1}$$

where c is the speed of light, $\mathbf{k}$ is the wave-vector, and $\hbar$ is the reduced Planck's constant. By momentum conservation, any photon refracted or reflected on the sphere will impart a momentum to the bead, according to the vector sum

$$\mathbf{p_{in}} = \mathbf{p_{out}} + \delta\mathbf{p_{bead}} \quad , \tag{3.2}$$

with $\mathbf{p}$ indicating photon momentum and $\delta\mathbf{p}_{\mathbf{bead}}$ the momentum added to the bead. Ashkin used a focused laser operating in the first Transverse Electro Magnetic mode (TEM_{00}), where the beam profile approximates a Gaussian intensity distribution and the electric and magnetic oscillations are transverse to the traveling direction. By this method, he was able to manipulate the spheres inside a fluid solution with one laser and control the full spatial position of beads by using two lasers, as seen in figure 3.1.

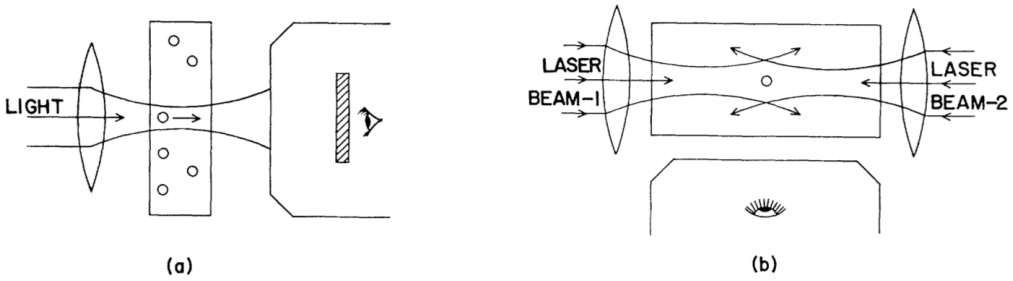

Figure 3.1: Schematic for the acceleration of micrometer particles as achieved by Ashkin in 1970. a) The single beam capable of accelerating particles toward the beam axis and scattering along the beam propagation direction. b) Confinement of a single particle using the gradient force to keep the particle in the center of the beam axis, and scattering force from two lasers to keep the bead in the scattering potential well between the two laser foci. Figure adapted from [18].

Again in 1986, Ashkin was able to improve on the single laser beam trapping, accomplishing full xyz-trapping for beads in solution[19]. This was made possible by sharply focusing a Gaussian laser beam, letting the forces due to refraction to be able to exceed the scattering forces near the focus. The total energy potential near the focus now had a minimum larger than the thermal forces available, that would push the bead out of the focus.

Ashkin found that possible trapping sizes ranged from 25 nm to several tens of micrometers. The general property required of the beads, is that they should be as transparent to the laser as possible, to offset the scattering forces compared to the refraction forces.

For optical trapping, there in general are two models for the forces experienced by a spherical particle. If the size of the particle is much larger than the wavelength ($d \gg \lambda$), the light can be described as optical rays refraction and reflecting on the object. This is referred to as the Mie regime, not to be confused with the Mie theory chapter in this thesis.

In the reverse condition, if the particle size is much smaller than the wavelength of light used for trapping ($d \ll \lambda$), the bead can be approximated as a point dipole and

the interaction of bead and beam can be examined by Maxwell's equations. Rayleigh scattering is the preferred model for this size-ratio.

Most current biophysical experiments using optical tweezers employ polystyrene beads at a size of about a micron to a few microns. The size of the bead to be trapped is thus similar to the wavelength of the trapping laser ($d \sim \lambda$), as most experiments use near infrared lasers, mainly with laser emissions at 1064 nm. This intermediate regime is of considerable interest due to the low absorbance of water[12] at the near infrared, thereby damaging any biological sample suspended in water solution as little as potentially possible.

3.1.1 Ray optics regime

The conceptually simplest of the models is reached in using the ray optics approach, as the light can be considered as linear ray traces, with no complications of a wave-model. Refraction of light in the latex spheres requires a higher index of refraction of the object to be trapped in respect to the fluid medium it is in, otherwise the object will be expelled from the beam due to inversion of the refractive forces. For a spherical bead with these quantities, the rays from a highly focused Gaussian beam refract in the bead as shown in figure 3.2. On refraction in the bead, momentum is added to the bead as seen by the red arrows. The difference in the Gaussian beam profile intensity is what allows the optical trapping, and the force arising due to the refraction is known as the *gradient force*.

The refraction angle for a ray of light entering a volume with a different refractive index than the one it was previously traveling through, is described by Snell's law as

$$\frac{\sin\theta_1}{\sin\theta_2} = \frac{n_2}{n_1} \quad , \tag{3.3}$$

where θ_1 is the angle of the incident and refracted ray θ_2, respectively to the interface surface normal vector. The refractive indices of the volume in which the incident and refracted rays travel are given by n_1 and n_2.

Scattering forces on the bead are caused by the angle dependent transmission and reflection, which are accurately formulated by the Fresnell equations. The polarization direction of the oscillating EM-field is a key factor in how an interface reflects and transmits, with the reflection of light having the polarization of the electric field in the same plane as the interface surface normal as

$$R_{\parallel} = \left[\frac{n_1\cos\theta_2 - n_2\cos\theta_1}{n_1\cos\theta_2 + n_2\cos\theta_1}\right]^2 \quad , \tag{3.4}$$

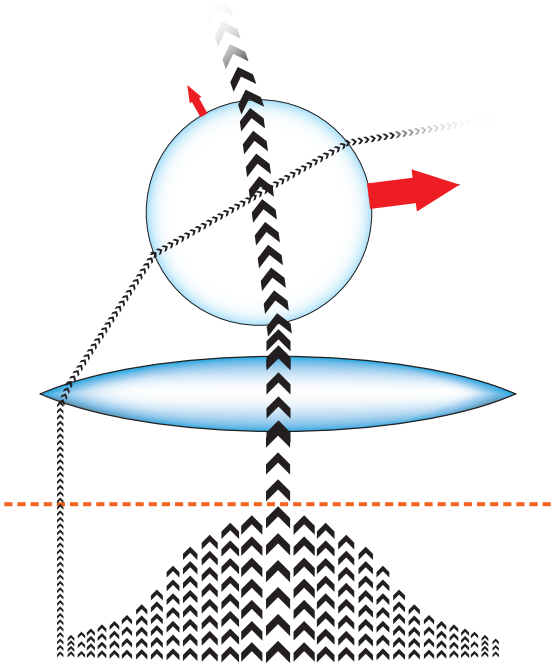

Figure 3.2: Gradient forces exerted on a spherical bead by a focused Gaussian laser beam, in the ray optics regime. At the bottom the whole beam profile is seen, with the thickness of the lines corresponding to the intensity at that radial distance from the beam symmetry axis. Above the dotted orange line, the optical paths for two rays are shown: one from the max. intensity center and one from the outermost low intensity part of the Gaussian beam. As they are focused by the objective lens, the incident rays are refracted in the bead resulting in two forces. The red arrows indicated the contribution from the two rays, with the total force pointing toward the center of the beam axis.

and if the electric field polarization is perpendicular to the one for $R_{\parallel}$, the reflection is

$$R_{\perp} = \left[\frac{n_1 \cos\theta_1 - n_2 \cos\theta_2}{n_1 \cos\theta_1 + n_2 \cos\theta_2}\right]^2 \quad . \tag{3.5}$$

The remainder of the ray is then transmitted into the new volume as $T = 1 - R$, maintaining unity for the optical ray when hitting the interface.

The intensity for a ray from the incoming focused Gaussian is focus-angle dependent as seen in figure 3.2. The momentum of a ray heading toward the focus of the trap can be defined as

$$\mathbf{p_{ray}} = \frac{n_1 P(\chi)}{c} \quad , \tag{3.6}$$

where $P(\chi)$ is the power at the focus-angle χ from the objective, where the most highly focused parts have a lower power than the center portion of the beam.

Forces due to both reflection and refraction can be split into two components[20, 21], a direction dominated by scattering which point in the beam propagation as

$$\mathbf{F_{sca}} = \mathbf{p}_{ray}\left[1 + R\cos 2\theta_1 - \frac{T^2[\cos(2\theta_1 - 2\theta_2) + R\cos 2\theta_1}{1 + R^2 + 2R\cos 2\theta_2}\right] \quad ; \tag{3.7}$$

and another which is the gradient force toward the beam center as

$$\mathbf{F_{grad}} = \mathbf{p}_{ray}\left[R\sin 2\theta_1 - \frac{T^2[\cos(2\theta_1 - 2\theta_2) + R\cos 2\theta_1}{1 + R^2 + 2R\cos 2\theta_2}\right] \quad . \tag{3.8}$$

Here the notation is as previous, with the R and T light polarization dependent. These forces due to single rays can be summed over the trapping beam and sphere, to reach the total forces due to the complete Gaussian beam.

For this model the resulting scattering and gradient forces are seen in figure 3.3, with parameters as listed in [20]. The total forces in both z and x direction are symmetric in magnitude around the trap center, but point toward the focus point. This constitutes the full optical trap, notably with a near linear relation of displacement to force for small displacements - as is the case for a harmonic potential. This is an important result for the practical applications of optical tweezers, where an external force acting on the bead can be quantified accurately if the position is known.

3.1.2 Rayleigh regime for dielectrics

In the case where the object is very small in comparison to the wavelength, the electric field from the wave of light across the objects linear dimension can be considered constant. This will allow a dipole interpretation of the objects electric response, or its polarizability α, to the external field $\mathbf{E}$ with an induced dipole momentum $\mathbf{p}$ as

$$\mathbf{p} = \alpha\mathbf{E} \quad . \tag{3.9}$$

The polarizability for spherical dielectrics can be described[7] as

$$\alpha = 4\pi r^3 \frac{\varepsilon - \varepsilon_m}{\varepsilon + 2\varepsilon_m} \quad , \tag{3.10}$$

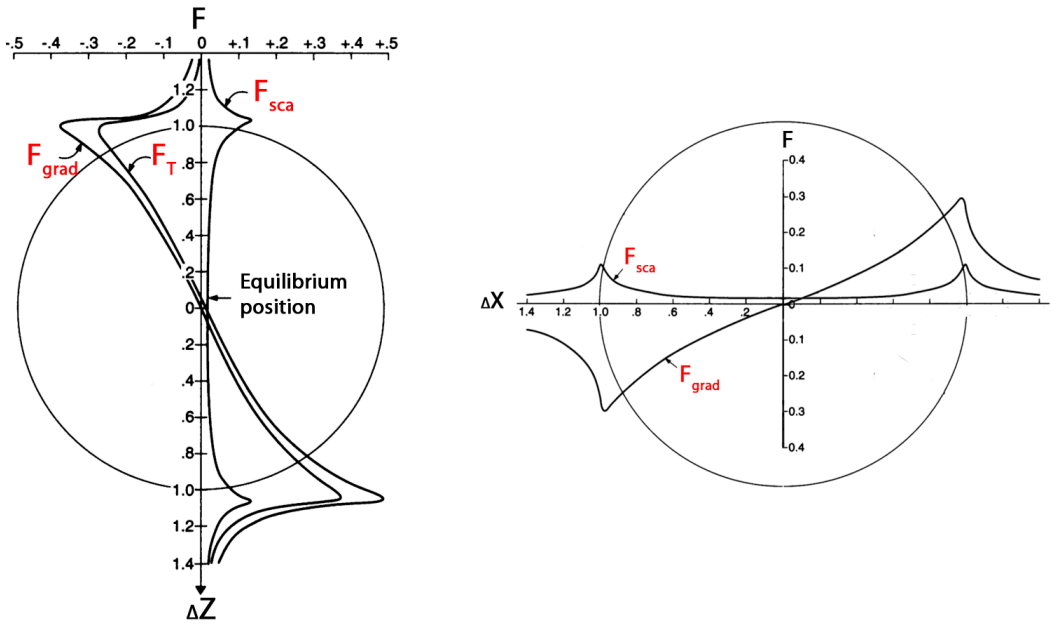

Figure 3.3: Model forces of scattering, $\mathbf{F_{sca}}$, and of gradient force, $\mathbf{F_{grad}}$, acting on a sphere at the trap focus giving the total force, $\mathbf{F_T}$. Left: Forces as functions of displacement in the z-direction. Right: Forces due to displacement in the x-direction. There is an equilibrium position in both of the two orthogonal directions, giving a stable optical trap. The circle indicates the bead radius. Figure adapted from [20].

with r the radius and ε the dielectric constant for the sphere and medium, ε_m. The dielectric constant is related to the complex refractive index N as

$$\varepsilon = N^2 = (n_{\text{ref}} + ik_{\text{ext}})^2 \quad . \tag{3.11}$$

The dipole moment is always induced with reverse polarity to the external field, this electrically oscillating point will then experience a force in the direction of maximum external field strength. As the Gaussian beam features such a gradient toward the beam axis, the dipole is situated in a potential described by

$$V = -\mathbf{p} \cdot \mathbf{E} \quad . \tag{3.12}$$

This potential will draw the dipole into the center of the beam with a force of

$$\mathbf{F_{grad}} = -\nabla V = \nabla \mathbf{p} \cdot \mathbf{E} = \alpha \nabla \mathbf{E} \cdot \mathbf{E} = \alpha \nabla \mathrm{E}^2 \quad . \tag{3.13}$$

As the polarization of the dipole is in the direction of the electric field of the trapping laser, the force on the particle is transverse to the beam axis - if the Gaussian beam is unfocused. The magnitude of this force is dependent on the gradient of the electric field of the Gaussian beam intensity distribution. If this beam is focused for optical trapping the gradient is as seen in figure 3.4, with the gradient force attracting the dipole particle toward the beam axis and focus.

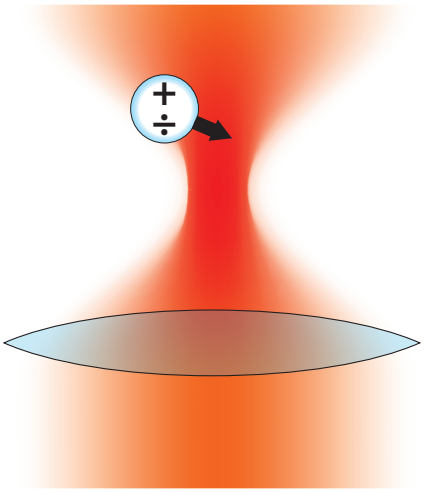

Figure 3.4: Time averaged electric field intensity of a focused Gaussian beam, indicated by color saturation. The particle is imparted an induced dipole momentum by the trapping laser, which attracts it in the direction of the electric field gradient.

Particles also experience a scattering force in the direction of the beam propagation axis. This is due to the elastic scattering of photons on the particle, where the contribution can be defined by the optical cross section for a particle size and optical properties, as seen in chapter 2. Scattering force on Rayleigh particles is modeled as

$$\mathbf{F_{sca}} = C_{\text{sca}} \frac{n_1 \langle \mathbf{S} \rangle}{c} \quad , \tag{3.14}$$

where $\langle \mathbf{S} \rangle$ is the time average Poynting vector for the beam and C_{sca} is the scattering cross section. The Poynting vector can thought of as the vector equivalent of the irradiance.

The scattering cross section for dielectric Rayleigh particles can be calculated as

$$C_{\text{sca}} = \frac{k^4}{6\pi} |\alpha|^2 \quad , \tag{3.15}$$

where k is the wave vector and α the polarizability.

The two forces are able to equilibrate near the focus point, if operating the laser with a high numerical aperture objective. The forces are not unlike those seen for the ray optics in figure 3.3, making optical trapping effective for small particles with high polarizability. Failure of trapping is a result of low α which scales with r^3, leading to a sharp cutoff in trapping strength, if equation 3.13 describes a force comparable to or lower than the thermal energy $k_B T$.

3.1.3 Rayleigh regime for conductive particles

For conducting materials, such as gold particles, the polarizability is restricted by the extinction depth of external electric fields. Svoboda and Block[22] estimate α for gold particles by the shell volume accessibly by the penetration depth δ of light on bulk gold by equation 3.10.

Higher precision is reached in deriving α using the Mie theory, where the dipole interaction is dominant as long as $d \ll \lambda$. The dipole polarizability for a conductive sphere[23] is given by the first electric Mie coefficient, a_1, alone as

$$\alpha = i \left[\frac{3r^3}{2x^3} \cdot a_1 \right] \quad , \tag{3.16}$$

with r the radius and x being the size-factor as detailed in chapter 2.

This can of course also be used to calculate the polarizability for dielectrics, although the Mie method is more complex in calculations. Calculations and the corresponding difference in polarizability by equations 3.10 and 3.16 are shown in table 3.1 for a gold

sphere of 200 nm size. The Rayleigh scattering overestimates the polarization by a factor of 100, while the phase-lag for both methods are of the same magnitude. Overestimation is a result of not properly considering the extinction in the sphere material.

Scattering cross sections are underestimated by the Rayleigh scattering, as is shown in comparison to Mie theory - just as expected, because Rayleigh scattering is only valid for very small particles with respect to the wavelength of light; while Mie theory is valid for all sizes.

Table 3.1: Comparison of α and C_{sca}, as determined by Rayleigh scattering for dielectrics and Mie theory, for a 200 nm gold sphere at 1064 nm wavelength light.

	Rayleigh scattering	Mie theory
α	1.4e-20 + i 1.2e-22	9.5e-22 + i 4.7e-22
C_{sca}	1.3e-14 m^2	5.9e-14 m^2

3.2 Optical trapping dynamics

Here the more practical properties for optical trapping are explored, by noting how the position of the trapped object is detected leading to a comparison for the movement expected by Stokes drag and thermal noise. Sample data for a trapped 1 micron polystyrene bead is shown for demonstration purposes, towards the end of this chapter.

It has been experimentally determined, that the position over time for a trapped particle in x, y, and z is that of a harmonic potential - both for Rayleigh particles[22, 24] and for micrometer sized particles[19]. This can be modeled as a Hookean spring, for the displacement Δx as

$$\mathrm{F} = -\kappa \Delta x \quad , \tag{3.17}$$

where κ is the optical trapping spring constant for the displacement from the potential minimum.

3.2.1 Position detection

After the focused Gaussian beam has passed its focus, the remainder of the beam can be recollected by another objective which re-collimates the beam. This beam is then allowed to hit an array of 4 photomultiplier diodes as seen in figure 3.5, attuned to the wavelength of the laser.

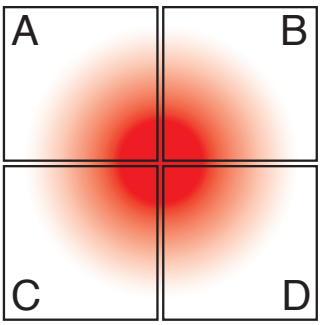

Figure 3.5: A Quadrant array of four Photomultiplier Diodes (QPD), with the surface aligned perpendicular to the beam directionality. The Gaussian is aligned at the center of the array, and any absorbed or refracted light by the object trapped at the focus, result in a diminishing of the intensity in one or more quadrants - and is directly related to the position of the object in the trap.

By aligning the Gaussian spot in the center of this array, the shadow cast by a trapped sphere lowers intensity in one or more elements of the array. It has been shown[25] that

because of the Gaussian gradient, the intensity losses in x and y are linearly proportional to the actual position of the bead relative to the trap center. This can be measured by the voltage differences as

$$V_x = \frac{(V_A + V_C) - (V_B + V_D)}{V_A + V_C + V_B + V_D} \quad , \tag{3.18}$$

and

$$V_y = \frac{(V_A + V_B) - (V_C + V_D)}{V_A + V_C + V_B + V_D} \quad , \tag{3.19}$$

with V_N as the voltages from the quadrants as shown in figure 3.5.

Further, in z-direction the shadow area is given by the ratio of the trapped bead cross section to the beam width at the z-position of the bead. So for z-position detection, the voltage loss of the entire array is proportional to the actual z-position of the bead, as

$$V_z \propto V_A + V_C + V_B + V_D \quad . \tag{3.20}$$

This position data is measured in Volts, and to relate this to the physical displacement in the trap it is needed to find a conversion factor, which can be accomplished by matching the distribution of the voltage signals to the Gaussian distribution expected for thermal random motion.

3.2.2 Brownian motion

A bead trapped in a fluid medium experiences a range of forces: the restoring force from the optical trap, the viscous drag as it moves, and the random thermal motion by the medium. The mean square displacement for a sphere[26] due to random thermal motion is

$$\langle \mathbf{s}^2 \rangle = 2Dt \cdot \mathrm{Dim} \quad , \tag{3.21}$$

with the time t, and Dim the dimensionality for the position vector $\mathbf{s}$. D is the diffusion coefficient as

$$D = \frac{k_B T}{6\pi\eta r} \quad , \tag{3.22}$$

a function of the Boltzmann constant k_B, the absolute temperature T, the viscosity η, and the sphere radius r. The denominator is the Stokes' drag coefficient, so k_BT acts a replacement for the velocity-term in the original Stokes' law:

$$\mathbf{F_{drag}} = 6\pi\eta r\mathbf{v} \quad , \tag{3.23}$$

where $\mathbf{v}$ is the sphere velocity. This equation is only valid for low Reynold's numbers, meaning only for slow motion of small particles so that the system inertia is negligible in comparison to viscosity.

The thermal noise present in the system is assumed to be random, and by Fourier transformation from the time-domain into frequency-domain, its value squared is

$$|\hat{F}(f)|^2 = 4\gamma k_B T \quad , \tag{3.24}$$

where f denotes the frequency and hatting indicates the Fourier time transform of the original function.

Returning to the motion of a sphere in a trap, the complete description is given by the Langevin equation as

$$F(t) = m\ddot{x} + \gamma\dot{x} + \kappa x \simeq \gamma\dot{x} + \kappa x \quad , \tag{3.25}$$

exploiting that the system inertia is ~ 0, and having the thermal random force as $F(t)$, and m the sphere mass.

On Fourier transformation of equation 3.25, it is gained that

$$\hat{F}(f) = (\kappa - 2\pi\gamma i f)\hat{x}(f) \quad , \tag{3.26}$$

By defining a corner frequency as $f_c = \frac{\kappa}{2\pi\gamma}$, equation 3.26 becomes

$$\hat{F}(f) = 2\pi\gamma(f_c - if)\hat{x}(f) \quad . \tag{3.27}$$

Real observables for equation 3.27 can be obtained by taking the square modulus and substitution by equation 3.24, so

$$\begin{aligned} |\hat{F}(f)|^2 &= 4\pi^2\gamma^2(f_c^2 + f^2)|\hat{x}(f)|^2 \\ |\hat{x}(f)|^2 &= \frac{|\hat{F}(f)|^2}{4\pi^2\gamma^2(f_c^2 + f^2)} \\ |\hat{x}(f)|^2 &= \frac{k_BT}{\pi^2\gamma(f_c^2 + f^2)} \quad . \end{aligned} \tag{3.28}$$

To clear up equation 3.28, the diffusion constant from equation 3.22 is invoked to give

$$|\hat{x}(f)|^2 = \frac{D}{\pi^2(f_c^2 + f^2)} \quad . \tag{3.29}$$

This equation describes the expected power spectrum of the thermal motion of a sphere of a given size, with f_c as the corner frequency containing the spring constant to be determined by fitting of experimental data.

3.2.3 Sample fitting

In order to concretize the previous section, the spring constant will be determined by fitting using sample data for a 1 micron bead in water. The data was kindly provided by Nader S. Reihani.

First, the position data is acquired as a time-series voltage signal as seen in figure 3.6. The position is seen as a set of discrete steps with varying magnitude, as expected based on the previous section. The harmonic potential minimum is here shown as the orange line for this short trace. The program used for fitting here is *Tweezercalib*[27].

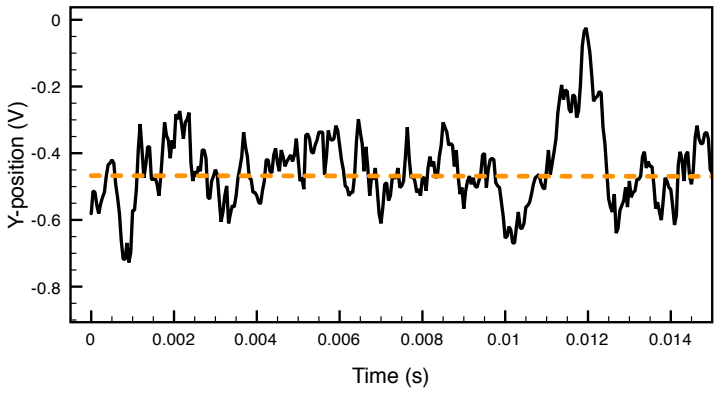

Figure 3.6: Position trace for y-direction of a 1 micron bead in water, the voltage position fluctuates around the orange mean value.

On transforming the entire 3 seconds long series into the frequency domain the power spectrum is gained as seen in figure 3.7. It is apparent that for low frequencies the optical trap is able to maintain the bead position, while for higher frequencies the trap restoring force is too slow to respond, letting thermal random motion rule.

The data set is smoothed and equation 3.28 is fitted to the power spectrum for the parameter f_c. As seen in figure 3.8, the fitted function accurately describes the data, with

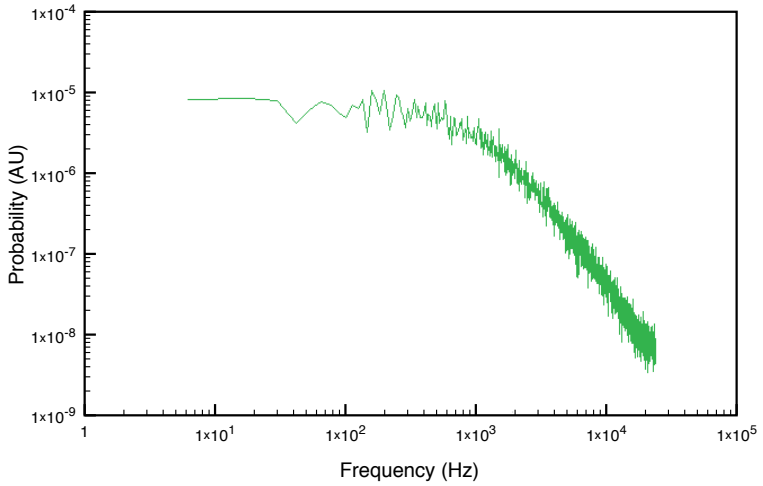

Figure 3.7: Fourier transformation of the trace seen in figure 3.6, showing the strong roll off past a certain frequency.

a found value of $f_c = 915Hz$. The trap strength is then directly given by $\kappa_y = f_c \cdot 2\pi\gamma$, and the found value can be used to relate displacement to force applied to the bead by using equation 3.17.

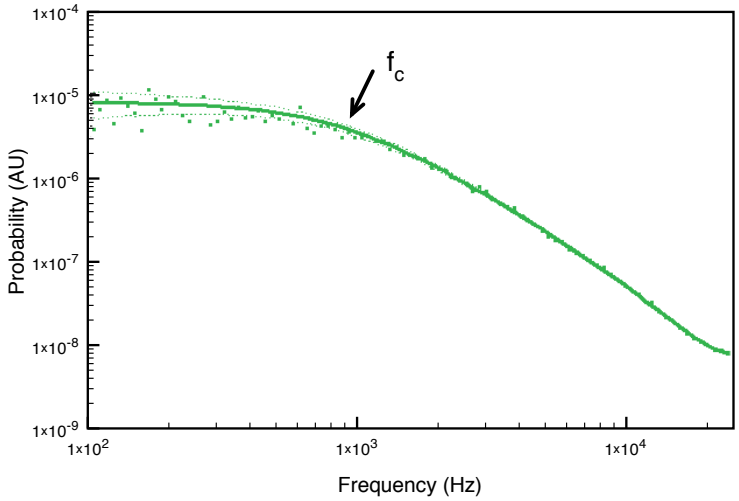

Figure 3.8: Fit to the Fourier transform, with the corner frequency marked as f_c.

3.3 Summary

The basic principles of optical tweezers have been investigated, with a focus on the forces that affect a trapped object. For gold particles, the polarizability based on Mie theory is seen as a direct factor for the gradient force; with the Mie scattering cross section a linear contributor to the scattering force. This will be used in the results chapter 6 to estimate the trapping strength of the gold particles as a function of their size.

Chapter 4

Phospholipid bilayers and phase transitions

All eukaryotic cells are bounded by a membrane, which primary function is to contain and separate the cell molecular machinery from the exterior environment. It also needs to function as a transport layer, for secreting extracellular components and byproducts of the cells metabolism, and ferrying of nutrients in the opposite direction.

In this chapter, the lipid bilayer formation and physical properties will be examined, with a focus on the possible use as a temperature sensitive probe for the heating of a gold nanoparticle.

4.1 Lipid chemical structure

The membrane consists for a large part of lipids, self organized into a double layer whose thermodynamical properties are determined by the lipid chemical structure. For many mammalian cells, one of the main lipid is phosphatidylcholine, which consists of a hydrophilic head-group with a double chain of hydrophobic hydrocarbon. An example for a chain length of 15 carbon atoms is shown in figure 4.1.

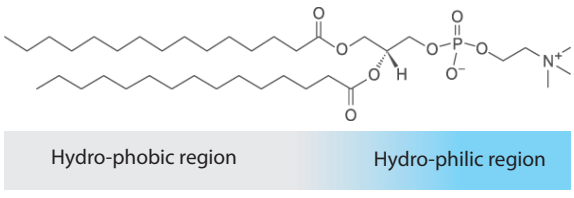

Figure 4.1: Structure of 1,2-dipentadecanoyl-sn-glycero-3-phosphocholine ($DC_{15}PC$), with indications of hydrophilic and hydrophobic regions.

The nature of phospholipid interactions is based on the different thermodynamic properties of these two regions, where the chains are uncharged as a whole; with a highly polarized phosphate-choline headgroup. In considering this single lipid's interaction with a highly polar solvent such as water, the solvent will assemble a solvation-shell around the polar headgroup, thus aiding and enhancing its solubility. Water will tend to avoid the oil-like double hydrocarbon chain, but there is still a partial pressure from the water causing the two chains to stick to each other.

On adding more of the same lipid to the water volume, the chains from each lipid will tangle up with those from another lipid - with the energy to drive the process originating from the high energy state of a water surrounded hydrocarbon chain. These lipids will aggregate with their tails tucked away from the water as seen in figure 4.2, where they self-organize into a small ball.

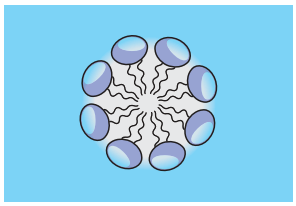

Figure 4.2: Micelle of phospholipids, the lipids are seen as headgroup blobs with chains pointing away from the solvent. The local water presence is indicated by the light blue color, with almost no water inside the micelle interior.

4.2 Lipid macro structures

On further increasing the lipid concentration, a point is reached where the lipids incorporated into micelles have a lower energy state if grouping into a locally flat structure, the simplest of which is the free lipid bilayer. This is a 2D sheet with a thickness of two lipids with their chains pointing towards each other, as seen in figure 4.3. The bilayer sheet is solvated and this regular assembly possesses many of the properties expected of a two dimensional fluid, such as lateral diffusion and viscosity.

Artificially created phospholipid bilayers are of importance due to the accurate mimicking of the cell membrane, while chemically simple, regularly ordered and smooth on the hundred nanometer scale. Depending on the ionic strength of the solvent and so the Debye screening distance, thermal undulations of two parallel sheets keep them from approaching and sticking to each other. The ends of bilayer sheets are not exposed to the water, as would be the case if figure 4.3 illustrated the whole of the sheet. Instead, the ends are thought to be capped with the lipid sheet presenting headgroups towards the water-interface, as seen in figure 4.4.

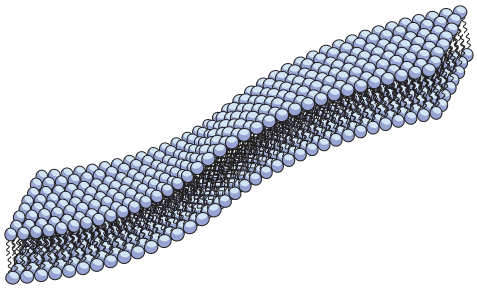

Figure 4.3: Section of a lipid bilayer, the polar headgroups are oriented to shield the internal hydrocarbon chain layers.

Lipid sheets are mechanically soft and easy to bend, with the energy required to bend a DCPC bilayer to a sphere on the order of 500 k_BT[26], with a low shear deformation resistance as expected of a 2D fluid. The energy needed for a lipid sheet to form smooth round edges is not inconsiderable and grows with sheet area. However, the bending energy needed to make a sphere out of a planar sheet is constant, so at some sheet size it is favorable to exist as a sphere with no edges; rather than a bounded sheet area. This macro structural conformation is illustrated in figure 4.4

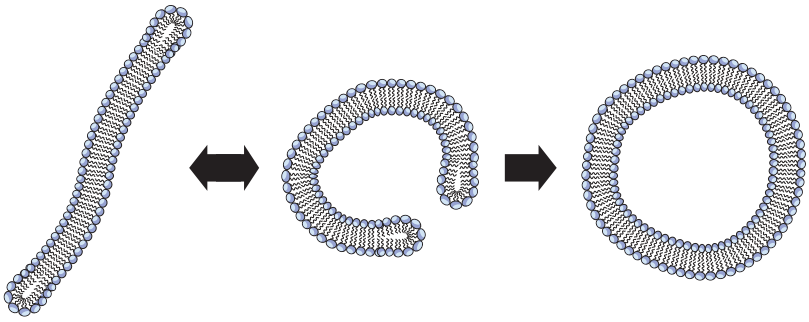

Figure 4.4: Thermal undulations of the lipid bilayer bring the edges close enough to allow them to anneal into a vesicle. Past a certain number of lipids in the bilayer, the most stable energy conformation is the continuos surface of a vesicle.

4.3 Bilayer phases and compression

Chemically pure lipid bilayers exist generally in two phases of matter when solvated in water, depending on the temperature with a narrow 1-2^{o}K transition between states. Both states are dependent on the chain interaction between lipids, as well as the chain

entropy. The lower temperature state is the *gel state*, where energy in the system forces the chain lengths to align in a crystalline array, with a high space packing factor. With increasing temperature, the heat capacity can not go higher while retaining the 2D crystal structure. Instead, the chain sections break into a higher entropy state, with no large scale ordering of chains lipid-to-lipid. This new state for the lipids, the *fludic state*, allows for more energy in the system and movement of lipids - the diffusion constant in the bilayer is higher than for the gel state. The two states can be seen in figure 4.5 with an intermediate of coexistent phase regions. The transition temperature, or melting temperature, is indicated as T_m.

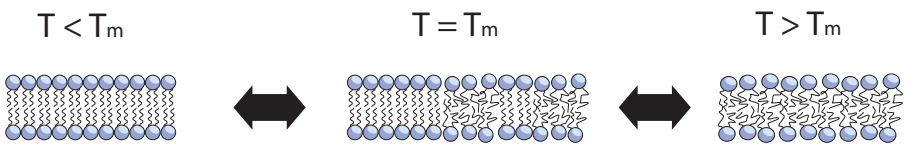

Figure 4.5: Transition of a lipid bilayer from gel phase into an intermediate with mixed domains. On further increasing temperature, the bilayer enters the fluidic phase with higher diffusion in the membrane.

Forces acting on the sheet in the in-plane direction can be seen as a lateral compression of the lipids. The energy needed to make a change in area for a bilayer can modeled as a function of the area compression modulus K_A[28] as

$$\Delta F(A) = K_A \frac{\Delta A^2}{A} \quad . \tag{4.1}$$

Here, the free energy increase is dependent on the area A and area change ΔA. K_A is then a measure of the energy required to compress or expand a sheet of lipids. It has been determined[29, 30] that this modulus is inversely linear to the heat capacity c_p for lipid bilayers, as

$$K_A = \frac{1}{c_p} \frac{A}{\gamma_A^2 T} \quad , \tag{4.2}$$

where T is the absolute temperature and γ_A is an experimentally determined constant.

The heat capacity for lipids exhibits a large increase at their gel to fluid phase transition, inherently because of the energy needed to break the orderly gel phase into the free planar fluid. $DC_{16}PC$ vesicles have been examined by Heimburg[29] and found to have a sharp transition point as seen in figure 4.6.

So at the heat capacity maximum there is at least a 100 fold decrease in the energy required to make a given area change of the bilayer. Locally on the bilayer, area changes

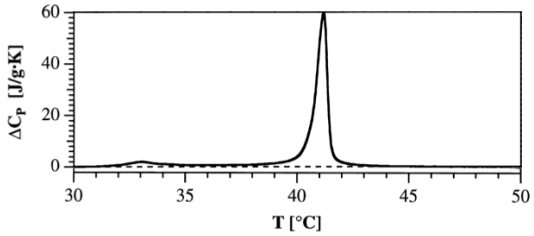

Figure 4.6: Calorimetry of $DC_{16}PC$ vesicles. Figure adapted from [29].

are then much more likely to happen due to thermal motion alone.

4.4 Permeability of bilayers

Above and below the lipid melting point, bilayers are normally impermeant to most water solubles and form a closed surface. Upon approaching the phase transition point, the local area fluctuations and low energy required to compress the bilayer increase the likelihood of spontaneous occurrences of small holes in the membrane. These holes are transient in the region of tens of milliseconds[30], but large enough ($\sim$ 1 nm) to allow for passage of small molecules. This is even more pronounced if driven by a potential, that forces the pores to become slightly larger.

Blicher[30] has directly shown the correlation between heat capacity and the rate of permeability of the lipid bilayer for the fluorophore dye Rhodamine. There is a marked increase in the porosity of the bilayer at the phase transition point, as shown in figure 4.7. This allows a net passage of components across the membrane, if a component is driven by a potential over the bilayer. For example, a difference in concentration would cause a force due to the equilibration of entropic partial pressure.

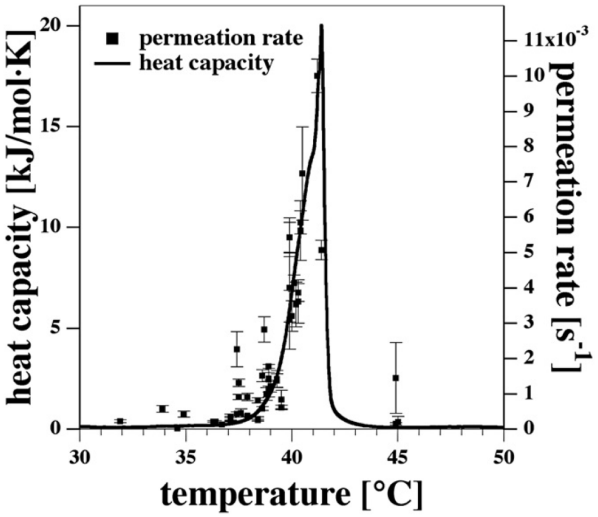

Figure 4.7: The permeability and heat capacity of the lipid bilayer, as a function of temperature. There is a direct relation of heat capacity to the porosity of the bilayer. Original figure from [30].

4.5 Phase dependent partitioning of fluorophores in lipid mixtures

The phase transition temperature for lipids assembled into bilayers depend on the chain chemical structure. In bilayers containing a mixture of lipid components, there may be more than one phase transition. For bilayers containing a small percentage of a new lipid species, the phase transition of the bulk lipid is the dominant and the new lipids cause only a minor perturbation to the phase transition. If for example, the new lipid has a lower melting point than the main lipid, it will prefer to be present in fluidic domains at the phase transition temperature for the main lipid. If it has a melting point above the main lipid transition, it will thus prefer to be present in a gel phase.

A requirement for this phase preference is that there is indeed both fluidic and gel phase domains available to diffuse into or out of. This can be satisfied either if the whole bulk bilayer is at its transition point, or if the bilayer is subjected to a temperature gradient so that it is split into two macro-scale domains. This is performed by Bendix[31], for a bilayer with minor parts of a lipid-fluorophore. One experiment with a minor part lipid with a T_m above; and one with a lipid with a T_m below the main lipid phase transition. This causes a partitioning of fluorophores as illustrated in figure 4.8.

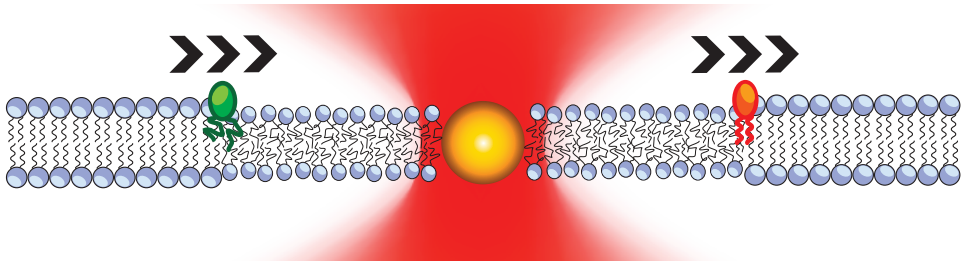

Figure 4.8: Lipid bilayer with a gold particle on a surface, near the focus of an optical trap. The heat from the gold particle induces a fluidic domain near the particle. The green lipid fluorophore has a melting point below the main lipid T_m and so it partitions into the fluidic domain. But, as the red fluorophore lipid has a higher melting point than the main lipid, it prefers the gel phase domain. Not drawn to scale.

Confocal fluorescent images from the original article is shown in figure 4.9, where figure 4.9b corresponds to the case for the green fluorophore lipid in figure 4.8, while figure 4.9d is illustrated by the red fluorophore lipid in figure 4.8.

Both the main bilayer lipid and the fluorophore conjugated to lipids seen in figure 4.9b are the same as those which are in this thesis, as described in chapter 5. This partitioning will be relevant for the detection of the phase transition in experiments, with the possibility of observation through confocal microscopy.

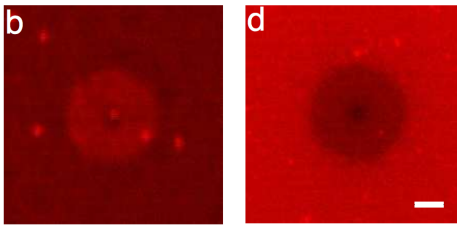

Figure 4.9: Confocal fluorescent images of a surface supported lipid bilayer with fluorophores incorporated. For both images, the very center contains a gold particle under 1064 nm irradiance. For b), the fluorophores are light chain, compared to the bulk bilayer lipid and prefer the induced fluidic domain near the gold particle. In d), the fluorescent dye has a longer chain than the bulk lipid, and prefer the gel phase domain further from the gold particle. Figure adapted from SI of [31]. Bar is 2 microns.

4.6 Summary

The permeability of lipid vesicles demonstrate their usefulness in acting as temperature sensitive probes, with the porosity acting as an indicator for the phase transition. Another possibly detection scheme is the local partitioning of lipid conjugated fluorophores, due to the simultaneous existence of gel and fluid domains. This may serve as a second phenomenon to be watched for in experiments.

The final concept of a vesicle acting as a probe can be seen in figure 4.10, where the interior of the vesicle is loaded with a dye that leaks through the membrane at its phase transition.

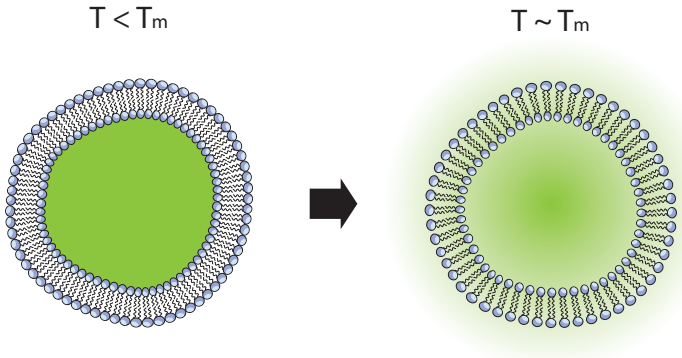

Figure 4.10: Leakage of the volume of a vesicle to the exterior, caused by the porosity of the bilayer at the melting point temperature.

Chapter 5

Experimental

Here, the details of the working setup for the experiment, with a focus on the experimental design and optical methods will be given. This provides an entry point to the interpretation of the results.

5.1 Confocal fluorescent microscopy

Fluorescent microscopy has long been a chief tool for molecular biology and biophysics, ideally offering a high positional resolution of conjugated biomolecules and membranes. While very much used through literature, it is hampered in its ability to resolve individual molecules due to out of focus returned light. For classic wide-field microscopy, the image is formed from the whole depth of field for the objective lens. This, in effect, results in a 2D projection of a volume, where the depth around the focal plane is approximately $0.5 - 1$ micron. Blurring from outside the focal plane leads to a degradation of the image clarity.

Confocal microscopy eliminates much of this overlay from volumes below and above the focal plane, by physical insertion of a pinhole in the light path exactly where the returned light from the objective intersects, shown in figure 5.1. This results in a lower amount of captured light, but this offset is often worth the resolution improvement. By this method it is possible to reach a diffraction limited image[32] of a sample, with much improved clarity for sub micron structures. Focal plane resolution is limited to about half the wavelength used to create the image.

Imaging speed is a limitation of the technique because in order to fully employ the potential benefits, the sample needs to be scanned in a sequential manner to form an image. The area to be imaged can be split into an array of pixels. By then scanning the excitation light in the same confocal manner as the capture of photons, it is possible only to excite and image a diffraction limited volume.

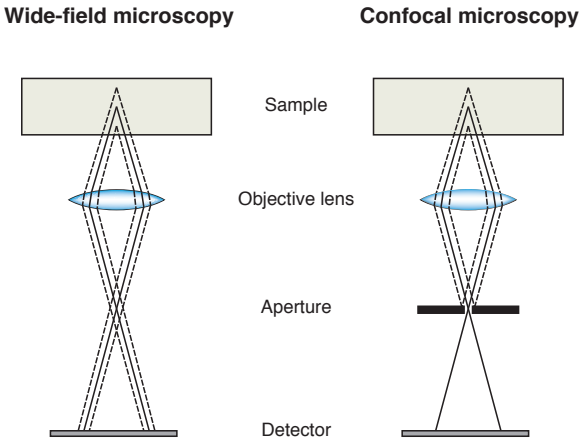

Figure 5.1: Principle of standard wide-field microscopy compared to confocal microscopy. The inserted pinhole for the confocal light path removes all out of focus optical contributions, yielding a higher resolution in the z-direction.

This microscopy method lets fluorescent vesicle membranes be accurately resolved. Results from using a non-confocal approach would make analysis of the actual membrane position harder to determine. Hence, confocal fluorescent imaging is a pre-requisite for the successful outcome of the experimental work.

5.2 Optical setup

A Leica SP5 laser scanning confocal microscope was used for all measurements, modified to implement the trapping laser as seen in figure 5.2.

The Nd:YVO_4 trapping laser emits a 1064 nm Gaussian beam profile operating in continuous mode, hence the EM field is even and not 'chopped' as in pulsed mode lasers. The beam is then expanded to a size that slightly overfills the aperture of the objective, so that the laser gradient is distributed over the entire lens to maximize focusing. Spherical aberrations are kept constant in the sample by using a water-immersion objective[24, 33]. The tradeoff by using a 1.2 numerical aperture objective is worth the loss in resolution, because this water immersion objective causes significantly less spherical aberrations. Therefore, it is possible to trap inside the sample at various z-depths; compared to the very narrow z-working range of an oil-immersion objective.

The scanning laser system by Leica has the ability to confocally excite a diffraction-limited volume using emission peaks (488 nm in particular) from an argon laser and additionally from a helium neon laser. By scanning a resonantly driven system of galvanic mirrors the resulting image can be captured in a fast manner with high fluorescent

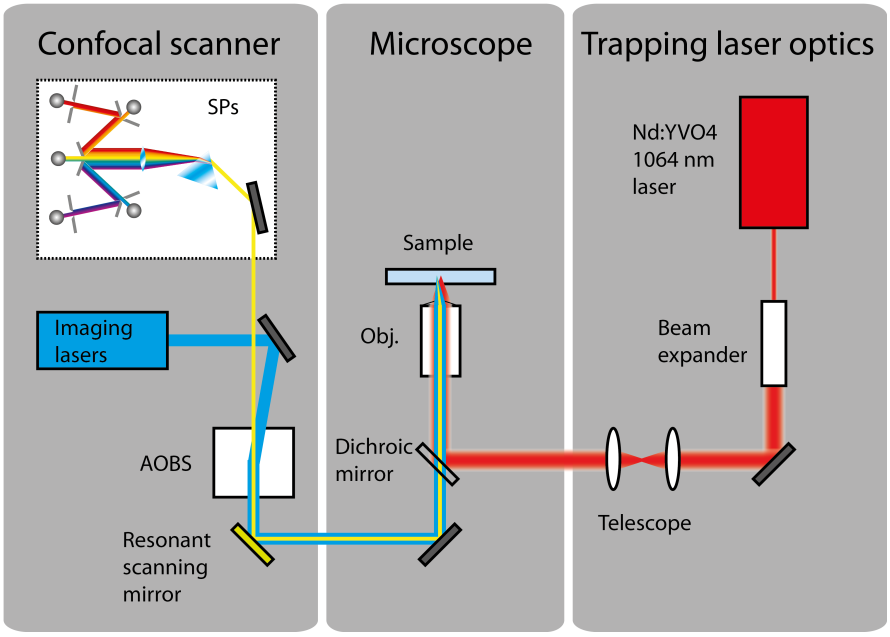

Figure 5.2: Optical setup showing all relevant parts. Confocal apertures are not shown.

efficiency. It is equipped with several SpectroPhotometers (SP) as seen in figure 5.2 with the ability to collect either backscattered or fluorescently re-emitted photons.

All emissions from the imaging lasers are individually tunable by the implementation of an Acousto Optical Beam Splitter (AOBS), with the returned light being separated in a prism and sorted for detection by SPs. This sorting is based on moving highly reflective razor-edge mirrors into the spectrally expanded return-light as seen in figure 5.2.

There was no need to use the photodiode setup usually associated with optical trapping as the fine movement of the trapped particle is not a concern; only the average position which is extracted by confocal imaging. As the gold nanoparticles are significantly below the resolution limit of the lens, they appear as dots with a Gaussian profile with a spread of about 300 nm. The standard deviation of motion in the imaging plane due to Brownian motion for a 60 nm gold particle at the laser powers used in these experiments, is

$$\sigma_x = \sqrt{\frac{k_B T}{\kappa_x}} = [0.5 - 1.7 \text{ nm}] \quad . \tag{5.1}$$

The numbers are based on the spring constants reported by Bendix[24] from trapping individual gold nanoparticles, using the same equipment as in the present work . Here, k_B is the Boltzmann constant, T is the absolute temperature in units of Kelvin and κ_x is the spring constant.

So, the position of a trapped gold particle is quite stable ($\sim$ 1 nm) compared to the distance error bars which will be presented in the results ($\sim$ 250 nm).

5.3 Experimental setup and procedures

The main plan for the experiment was to have a vesicle temperature probe on a non-interfering surface. Vesicles must be easy to visualize and a detection method for their phase transition is required. Key steps are illustrated in figure 5.3, with highlights of each step in the following paragraphs.

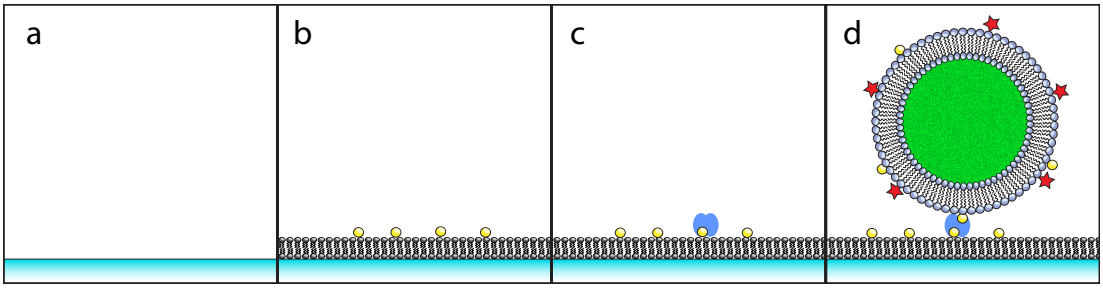

Figure 5.3: Sample preparation steps. a) Glass etching. b) Supported lipid bilayer tagged with biotin adsorbed. c) Neutravidin binding on biotin. d) Docking of giant unilammelar vesicles containing Alexa dye and a membrane bound Texas Red dye.

By having a Supported Lipid Bilayer (SLB) monolayer on the glass, the lipid vesicles for the experiment are buffered against adsorption onto the glass. The monolayer may also function as a docking plane for the vesicles, by using the well-described Biotin to Avidin binding[26]. The SLB lipid mixture is produced in a glass vial by addition of 1% mole weight Biotin conjugated DHPE lipid to 100% POPC lipid in chloroform, chemical structures can be seen in figure 5.4, left and center. The POPC main constituent has a chain phase-transition at -2^oC and is in the fluidic state for the experiment ambient temperature. By evaporating the chloroform solute from the preparation glass vial and placing it in vacuum for 2 hours, the lipids are deposited as multi-layer sheets on the glass wall with minimal residue chloroform[34]. The chloroform is an ideal solute for the polar and neutral parts of the lipids, as it allows free mixing with no macro scale ordering into sheets.

The sedimented lipids can now be hydrated with a Phosphate Buffered Saline (PBS) solution, at 0.1 M ionic strength: a biologically relevant ionic value, but low enough to avoid lipid aggregation through high Debye screening[26]. After being left overnight, all lipids are incorporated in solute vesicles with highly varying size. This solution is then pressed 9 times through a membrane extruder from Avanti Lipids at a filter pore size of 100 nm, which produces vesicles of a narrow size distribution centered at the pore size of the filter[35]. The tiny vesicles are brought into contact with a glass surface, netting

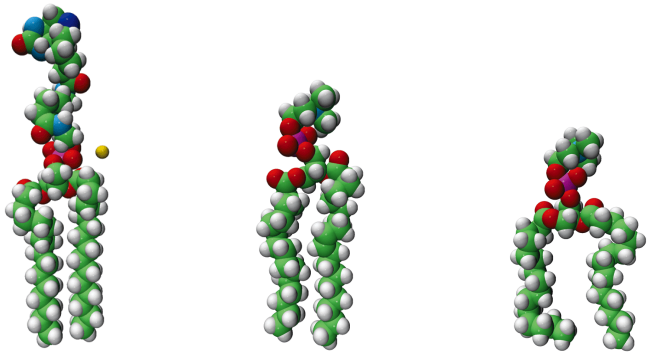

Figure 5.4: Chemical structure for (left) Biotin-DHPE, (center) POPC, and (right) $DC_{15}PC$ phosphor lipids; images by Avanti Lipids. Green indicates Carbon, white is Hydrogen, red is Oxygen, and blue is Nitrogen. Magenta is Phospor and yellow is free $Natrium^{+}$

a homogenous lipid monolayer surface[36]. The process of adsorption of the nano sized vesicles are suggested to be an edge-catalysed action[36].

It was found that it is necessary to have a highly charged surface in order to allow for a good adsorption surface for the lipids used for the SLB, a pre-requisite to achieve a good area coverage on the glass. To hydroxylate the raw glass surface and create a highly charged OH-group surface, the circular 0.14 mm thickness cover glass slides were prepared by immersion in boiling piranha solution for 30 min and flushed with Millipore water 5 times. Piranha solution is a 3:1 mix of conc. sulfuric acid and 38% hydrogen peroxide, which when adding the peroxide to the acid heats up to a slow boil as the acid spawns H_3O^{+} and free atomic oxygen. This highly corrosive and reactive solution eats away at organic residues and fully oxidizes the raw glass surface.

Treated glass is then placed in an aluminum sample chamber, with the glass at the bottom of this cage. A teflon o-ring with a rubber seal can then be screwed tightly onto the glass, as seen in figure 5.5, providing a minimally reactive surface while the hydrophobic teflon is ideal for quick flushings of the chamber. The height of the O-ring assembly is approximately 5 mm and the chamber can contain a volume of at least 500 μL. Now, SLB lipid solution is added at 200 μL to the glass in the sample chamber and left to adsorp overnight.

It is now necessary to remove excess POPC solution and prepare the sample for the main component of the experiment: the Giant Unilammelar Vesicle (GUV) probes. By washing first 10 times with 500 μL milli-pore water, most unruptured SLB vesicles are destroyed, diluted, and washed away. The solution can then be replaced by washing 5 times with 500 μL 0.1 M salt strength PBS. Neutravidin is added to a concentration of 0.02 M and left to settle for 5 min and washed again 5 times with PBS. The SLB now presents a neutravidin docking interface to be used with the probe vesicles.

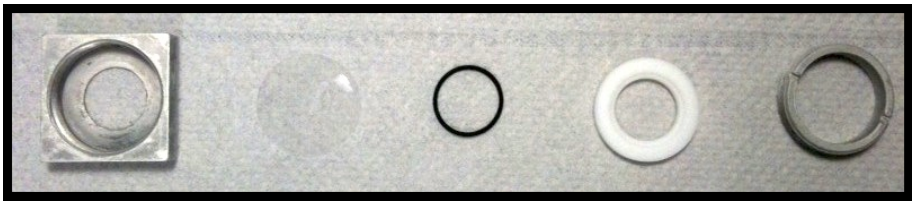

Figure 5.5: Sample chamber components, from left to right: main aluminium housing, glass slide, o-ring, teflon ring, aluminium compression ring.

The GUV temperature sensitive probes are formed using the same general guide-line as for the SLB lipids, but using sorbitol for hydration as it yields much larger vesicles[34]. The components are 100% $DC_{15}PC$ with 0.1% Biotin-DHPE, as seen in figure 5.4 center and right. Additionally, these vesicles contain a fluorescent red dye lipid component: Texas Red-DHPE at 3%, which is very photo stable and gives a high quantum photonic yield - perfect for detecting the bilayer membrane using confocal fluorescent microscopy. The major lipid of the GUV recipe, $DC_{15}PC$, has a narrow chain phase transition at 33^oC and by exploiting the permeability of the vesicle bilayer at this temperature, as detailed in chapter 4, it can be accurately determined when the membrane reaches the phase transition temperature.

Having the ability to detect the permeabilization is the key indicator for the phase transition in this work. Under the normal fluidic or gel phases of the phosphor-lipid membrane of this experiment, the water soluble fluorescent dye Alexa Hydrazide cannot penetrate to the probe vesicle membrane. The volume of the GUV's is loaded with Alexa 488 Hydrazide, as seen in figure 5.6, by thermal cycling past the melting point for the $DC_{15}PC$ lipids. This is ensured by letting vesicles pass by the phase transition temperature, while the solution outside contains Alexa fluorophore. Porosity at the phase transition then allows the Alexa Hydrazide to enter the vesicles, which are re-sealed by dropped the temperature to the ambient. Complete probe vesicles are then deposited on the SLB surface and excess un-docked vesicles and dye in the solution are washed away by PBS to enhance imaging contrast.

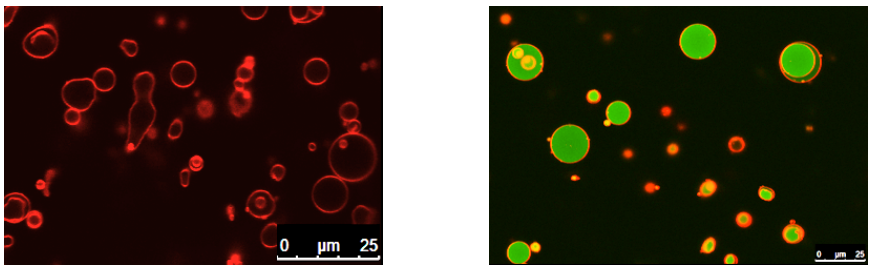

Figure 5.6: Confocal fluorescent images of giant unilammelar vesicles. Left: bare vesicles, with the membrane seen as red. Right: vesicle volume filled by Alexa dye seen in green.

For all experiments the sample was kept at 25^{o}C with a stability of 1 degree as measured by a thermistor probe in the sample solution. This corresponds to 8^{o}C below the phase transition point for the $DC_{15}PC$ vesicles.

Due to the charged surface left over from synthesis of gold particles[37], there is a need to shield the gold particles otherwise they will stick too much to vesicles and glass surface bilayer. The gold particles can be shielded by sonicating 450 μL from each stock solution by British Biocell International (60, 80, 100, 150, or 200 nm), and then adding 50 μL thiolated PEG from Aldrich Sigma at 5 mg/ml to each suspension and agitate at 1000 rpm for 30 min[38]. This will coat the gold particles in a blanket of polymer, capable of buffering the particle against the lipids present and preventing gold particle aggregation. Coated gold particles can now be added in small amounts to the final sample for optical trapping.

5.4 Image acquisition

Images are acquired using the Leica SP5 Advanced Fluorescence software, capturing at 512x512 pixels at a rate of 400 Hz leading to $\sim$ 0.8 frames per second. The Alexa 488 is excited at 488 nm from the scanning confocal laser with fluorescence received in the interval 495-565 nm; while the membrane bound Texas Red-DHPE is excited at 594 nm and imaged at 610-710 nm. The two fluorophores are well separated spectral-wise and minimal crosstalk is expected based on their excitation data, see appendix 8.2. The gold particles are strong scatterers of the 594 nm wavelength as surveyed in chapter 2, and so the backscattered light from the gold particles is collected in the range 589-599 nm.

By these parameters a clear image is resolved with simultaneous acquisition of the vesicle membrane, the volume of the vesicles, and the gold particles. The trapped gold particle is held in the z-plane of the vesicle equator by software refocusing, searching for the largest area of Alexa fluorescence, thereby the equator. By geometry, the determined distance from membrane to particle is then always larger or equal to the actual distance, as illustrated in figure 5.7.

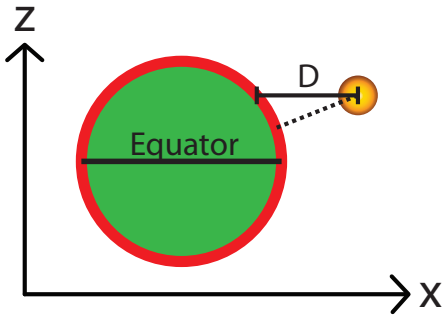

Figure 5.7: Geometry of the determination of the distance D, between vesicle membrane and gold particle. As imagining captures the xy-plane, the distance is determined parallel to this plane. For the worst case scenario as illustrated, the actual distance (dotted line) is shorter than the measured distance (D). By keeping the gold particle in the equator plane of the vesicle, the difference between actual and determined distance is minimal.

5.5 Piezo control

When a gold particle enters the trap, it is a requirement for high precision in the distance measurement to have a very stable piezo stage. In this work a P-517.3CL Physik Instrumente stage with capacitive feedback was used, claiming a resolution of sub 1 nm. The control interface gives precise XY positioning with velocity control for moving the stage.

In the experiments, the vesicle was moved at a constant rate of 10 nm/s toward the trapped gold particle.

Chapter 6

Results and discussion

This chapter contains the main results of the thesis. Also, discussions of the results and relations to literature are given.

6.1 Image analysis

The output data consists of 2 fluorescent signals: from the membrane and the lumen, as well as the reflection signal from the trapped particle. On overlaying these separate sources, the final image is created as seen in figure 6.1, which is an image from a movie.

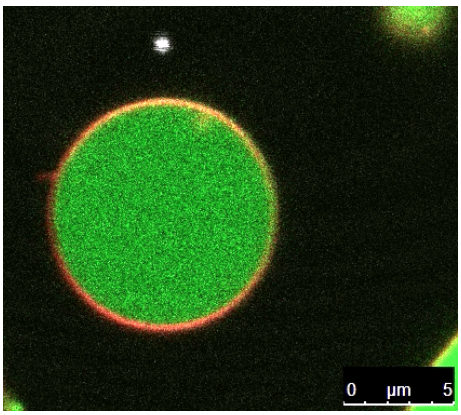

Figure 6.1: Snapshot from a typical experiment. The membrane is seen as red with the volume of the vesicle identified by the green Alexa membrane impermeant dye. The small white dot is the backscattering from the gold particle.

6.1.1 Leak detection

To correctly determine the leak distance, it is first needed to establish what a leakage phenomenon entails. If the area intensity of the volume of a test vesicle is plotted over elapsed time (and therefore over distance between gold particle and vesicle, as the piezo constantly moves the sample with respect to the trapped bead), the graph shown in figure 6.2 is obtained. In this experiment, the leakage and following decrease in intensity occur at around 45 seconds. The phenomenon is reproducible and fully reversible, in that the trapped particle can be withdrawn effectively stopping any leakage.

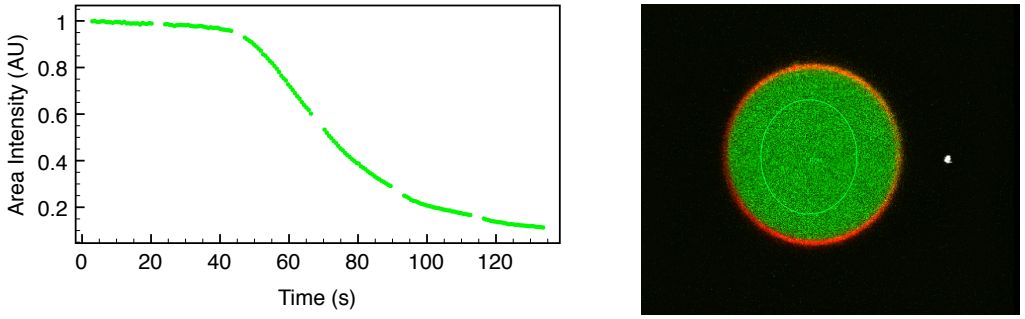

Figure 6.2: Left: Leak of volume confined Alexa 488 dye. The graph shows the area intensity for the marked part of the green volume in the right image. The gaps stem from the refocusing software, needed to ensure an orthogonal approach vector for the gold particle, see section 5.4.

Looking at the intensity curve for the Alexa Hydrazide dye, it seems there is first a linear plateau with no leakage - only minor photobleaching. After this there is a bend followed by another linear part, before rolling off as the Alexa dilutes into the solution. By fitting a line to the linear part before the first bend and another line to the linear part after the first bend, the leak event is defined to start at the time where the two linear fits intersect. In figure 6.3, fitting is performed on the data shown in figure 6.2. This protocol is easy to implement and robust, because all experiments exhibit this behavior, see the thick lines in figure 6.6.

The membrane bilayer will enter a mixed lipid state of fluidic and gel phase domains upon approach of the heated particle, when the temperature at the vesicle exceeds the phase transition temperature. This interface of lipid domains is highly in-plane compressible and allows permeability across the membrane for the dye inside the vesicle, as detailed in chapter 4.

Another interesting observation is that for the membrane bound Texas Red, an increased intensity is seen closest to the trapped particle, as shown in figure 6.4. This effect is probably caused by the fluorophores preferring to partition[39, 40] into the fluidic lipid domain. This property was used in the molecular sorting paper by Bendix[31]. It may also be caused by the gain in rotational freedom possible in the phase transition regime,

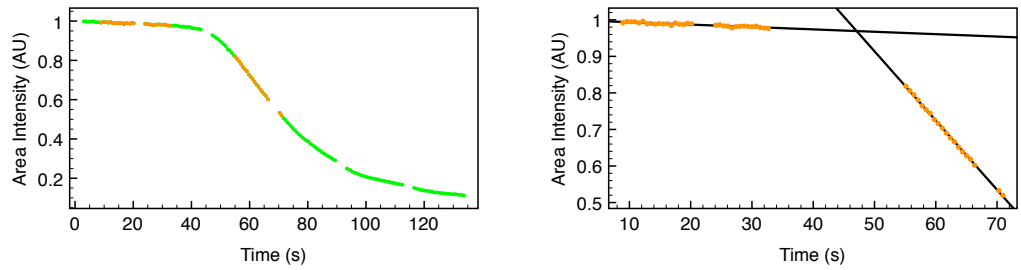

Figure 6.3: Demonstration of leak time determination by fitting analysis. Left: the linear orange parts of the data are cropped from the remainder. Right: these two linear parts are seperately fitted as the black solid lines, with the intersection at 47.1 s defining the leak time.

allowing the excitation dipole moment for individual Texas Red fluorophores a better alignment with regard to the polarization direction of the excitation laser. There is a static difference in intensity around the perimeter of the membrane with a periodicity of π as seen in figure 6.1. This is caused by the scanning direction of the confocal setup. Suppose the maximum intensity at the top and bottom represent an optimal alignment of the fluorophores in terms of dipole excitation efficiency, then approaching with a trapped gold particle at these ends should not increase fluorescence, given that an increase in rotational freedom should either result in the same or lower Texas Red excitation efficiency. However, experiments do show increased fluorescence in these parts as well, so the idea of increased signal caused by a higher alignment freedom can be discarded.

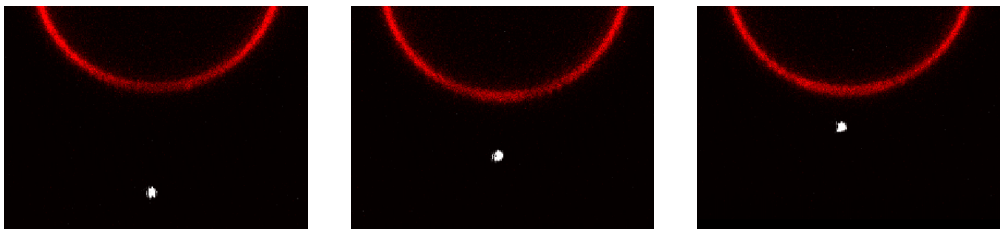

Figure 6.4: Fluorescent images showing only the red membrane signal. An increased fluorescence is seen near the gold particle as it approaches the vesicle. This is a local partitioning of Texas Red-DHPE into the fluidic domain.

Further, the two separate fluorescence phenomena are co-incident as shown in figure 6.5, which shows a decrease in volume signal and an increase in membrane signal within the box. This supports the correct detection of the critical particle-to-vesicle distance which leads to a sufficient temperature increase, such that the membrane undergoes a phase transition. The average of five independent experiments at the same parameters is also shown in figure 6.5, using the data presented in figure 6.6.

While the photo-diode was not used to record position data for the trapped particle,

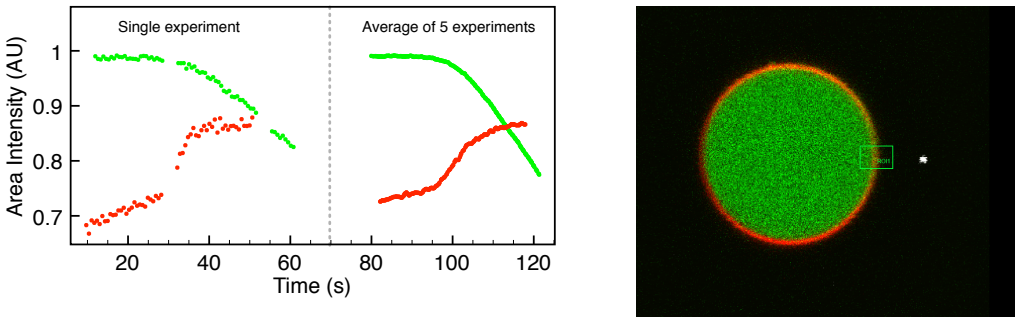

Figure 6.5: Alexa dye leakage and increased Texas Red fluorescence from the membrane area closest to the trapped gold particle, as a function of elapsed time. The graph shows fluorescent intensity for the area marked in the right image for the red membrane channel; the green signal originates from the area marked in figure 6.2.

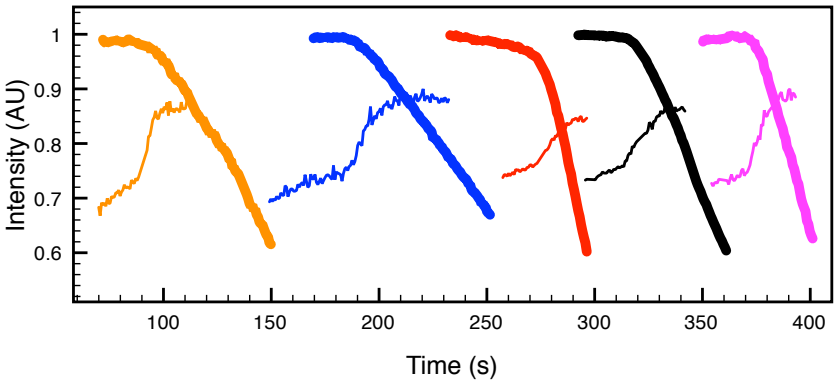

Figure 6.6: Leak events for 5 representative experiments, with each experiment represented by one color. The thick lines are the intensity from the volume of vesicles and the thin lines represent the intensity from the membrane closest to the trapped gold particle. The membrane and volume signal changes occur at the time the leakage starts. Data was shifted in time to allow side-by-side comparison between experiments. Refocusing gaps in the data were filled, to ease visualization.

there was still a need to obtain the position of the gold particle. This was achieved by measuring the intensity of backscattered 594 nm light at the trap image position and rejecting experiments with an uneven intensity profile as the one seen in appendix 8.3. Experiments that showed an abrupt bursting of the membrane were also discarded by the argument that the vesicle was weakly formed or otherwise defect.

At the time the phase transition exactly is reached, the distance from trap center to the membrane is measured manually using Leica software. For the gold particles, the center is defined as the center of the Gaussian intensity profile. The membrane position is defined as the Gaussian peak intensity when making a line plot, pointing orthogonally to the membrane from the gold particle. This distance is indicated in figure 6.7

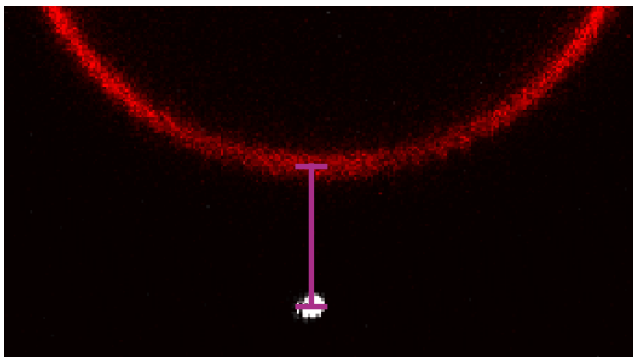

Figure 6.7: Definition of distance between gold particle and membrane. The magenta line starts at the center of the gold particle and goes directly to the membrane, where it ends at the intensity peak for the membrane.

6.2 Results

The data will here be presented in its raw form, this will be followed by modeling according to Mie theory, and finally there will be a general discussion.

Initially, the trapping laser power output was measured by dismounting the objective and measuring the energy flux for the beam just before entering the objective. It has prior been determined that for 1064 nm the transmission coefficient for the objective is 0.63 [41]. The resulting power in the sample is seen in figure 6.8. This will be used to determine irradiation at the focus and as a basis for comparison to literature in the discussion.

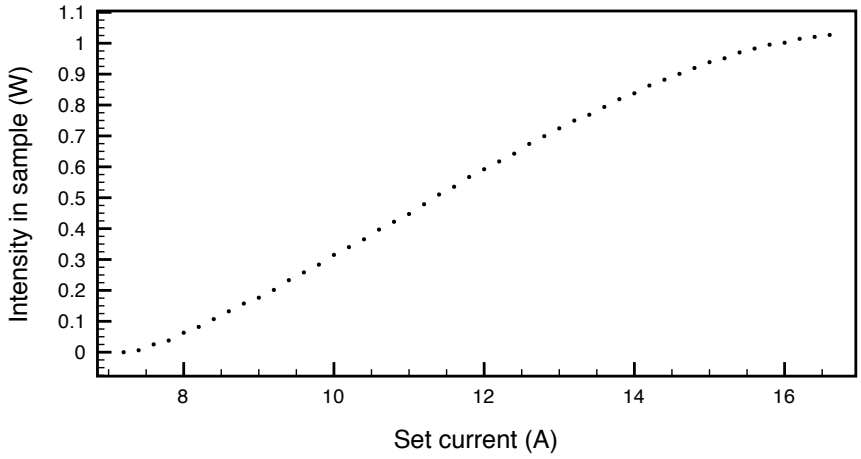

Figure 6.8: Calibration of power after 1.2 NA water objective as a function of the set value of current for the trapping laser.

6.2.1 Distance to induce chain phase transition

Each size of gold particle was trapped in 5 individual experiments at several laser powers. The distance needed to induce a phase transition event at the surface of a vesicle scales linear with power at the focus, as shown in figure 6.9. Between the gold particle sizes of 60, 80, and 100 nm there is a clear increase in the critical distance needed to reach the phase transition temperature for melting the vesicle bilayer. That there is a linear relation with input power fits well with the heat flow model developed by Goldenberg[42], which describes the heat flow from a sphere embedded in a medium, described with different heat conductive properties. The steady state limit of this solution states that

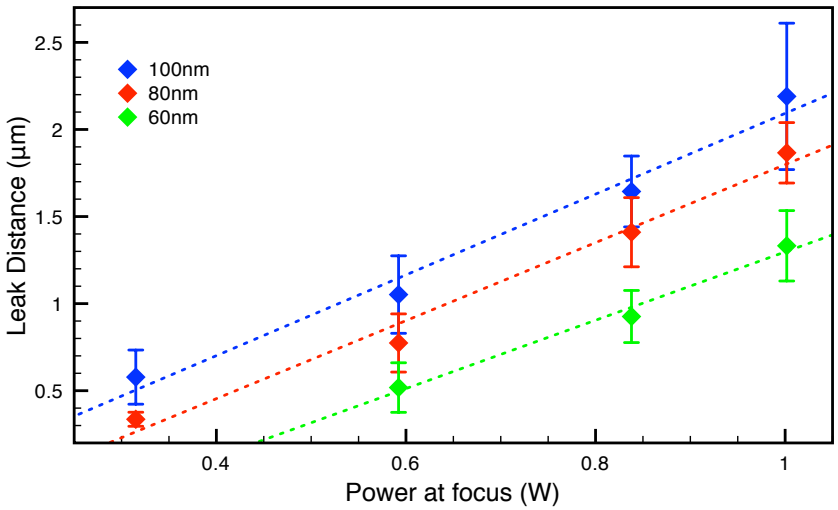

Figure 6.9: Experimentally determined leak distance for 60, 80, and 100 nm gold particles at a range of laser powers. There is clearly a linear dependency on trapping laser power output as seen in the lines, which are the linear fits to the individual sizes. Each point consist of 5 individual trapping experiments, with error bars denoting one standard deviation.

$$\Delta T_{\text{in}}(D) = \frac{Ar^2}{3K_w}\left[\frac{1}{6}\left(1 - \frac{D^2}{r^2}\right)\right] \quad , \tag{6.1}$$

$$\Delta T_{\text{out}}(D) = \frac{Ar^3}{3K_w D} \quad . \tag{6.2}$$

$\Delta T_{\text{in}}(D)$ is the temperature at a distance (D) from the sphere center and *within the sphere radius*; while $\Delta T_{\text{out}}(D)$ is valid for *distances larger than the radius* with respect to the sphere center. The radius of the sphere given by r and K_w is the thermal conductivity of water. A is the energy input density:

$$A = I \cdot C_{\text{abs}}/V_{\text{sphere}} \quad , \tag{6.3}$$

with I being the irradiance and V_{sphere} the volume of the heated sphere. C_{abs} is the absorption cross section, this can be calculated as shown in chapter 2 for modeling. The absorption cross sections for each size as determined by Mie theory result in the surface temperatures as functions of laser power, as seen in figure 6.10, while setting the irradiance as described in equation 6.6.

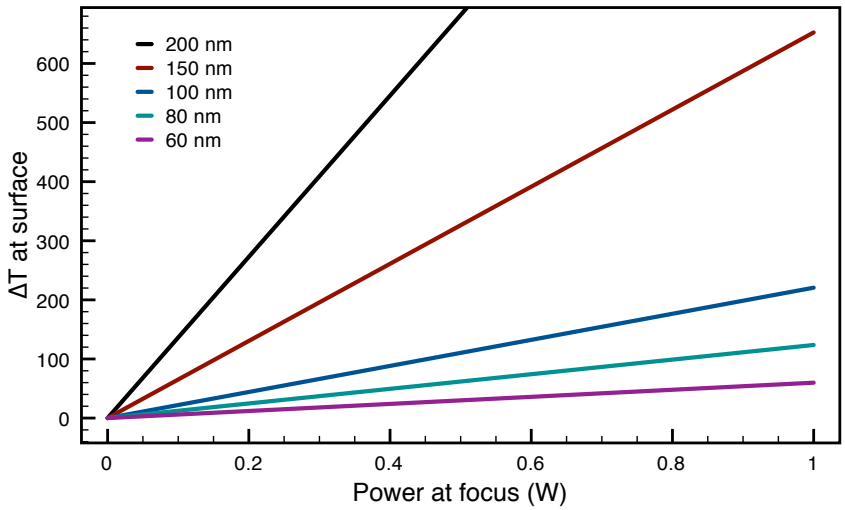

Figure 6.10: Surface temperatures for gold particles as functions of laser power, calculated based on Mie theory and the Goldenberg relation, with irradiance as detailed in equation 6.6.

Another possibility is to estimate the value for A from the experimental data and derive the surface temperature for the gold particle in question. If the temperature is known at a given distance, A is from equation 6.2

$$A = \frac{3\Delta T_{\text{out}}(D) K_w D}{r^3} \quad , \tag{6.4}$$

and by re-inserting this value of A into equation 6.2, the surface temperature can be obtained by letting $D = r$.

The distance required to melt the bilayer from equation 6.2, if ΔT is set to 8^oK, is

$$D(I, C_{abs}) = \frac{I C_{abs}}{32\pi K_w} \quad . \tag{6.5}$$

So that $D \propto I$ is seen both in the model and in the experimental data, as shown in figure 6.9, is further indication of the validity of the results.

We also have data for the gold particle sizes of 150 and 200 nm. Compared to the lower sizes there was a marked difficulty in trapping these large particles, as was also noted earlier by Bendix[24], where it was found that the trapping strength in the imaging plane was virtually the same for 100, 150, and 200 nm gold particles, as seen in figure 6.11. For smaller particles there is a clear scaling of the spring constant in the imaging plane by r^3. The leak distances as measured for 150 and 200 nm gold particles are seen in

figure 6.12, where each point is again an average of 5 experiments. For these sizes there are no overall linear tendencies, with an apparent leveling off for laser power over ~ 0.85 w.

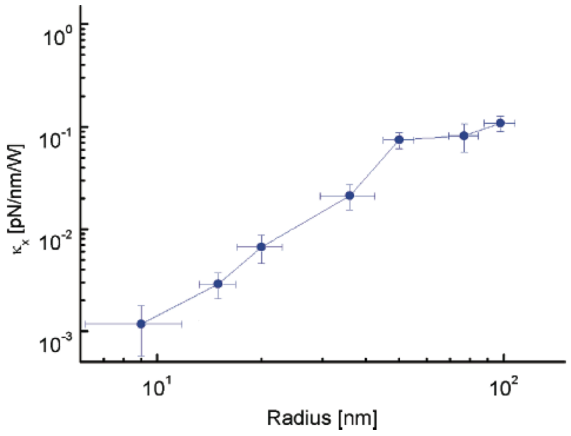

Figure 6.11: In-plane trapping strength for gold nanoparticles as determined by Bendix[24]. The 3 right-most values are for 100, 150, and 200 nm gold particles, and show that the difference in κ_x between these is very small compared to the difference between the sub-100 nm sizes. Figure adapted from [24].

The focused nature of the trap beam for the 1.2 numerical aperture objective means that a small change in z-depth from the narrowest beam waist, results in a large difference in spot size and therefore the power per area. A difference in trapping depth could explain the similar characteristics of the 100, 150, and 200 nm particles. There is however no simple way of determining the z-position of the trapped particle in respect to the focus. Ideas for this is suggested in the outlook, chapter 7.1.

A control for heating by the laser itself was conducted by moving an empty trap toward vesicles, with the result of leakage only when the trap focus was directly on the membrane. This also induced some deformation of the vesicle, due to sorbitol refractive index mis-match in respect to the water outside, leading to a partial interaction of the vesicles with the optical trap. Vesicles could be trapped in solution and showed no leaked while trapped. Occasionally, it was possible to move a trapped gold particle across the vesicle bilayer into the interior of the vesicle, without disrupting the membrane, see SI5 moviefile on the CD attached at the back of this thesis. For this control, the intensity profile for the Alexa dye is available in appendix 8.4, while trapping a gold particle inside the vesicle. This caused no effect on the fluorescent intensity of Alexa 488, except for the static photobleaching by the imaging lasers.

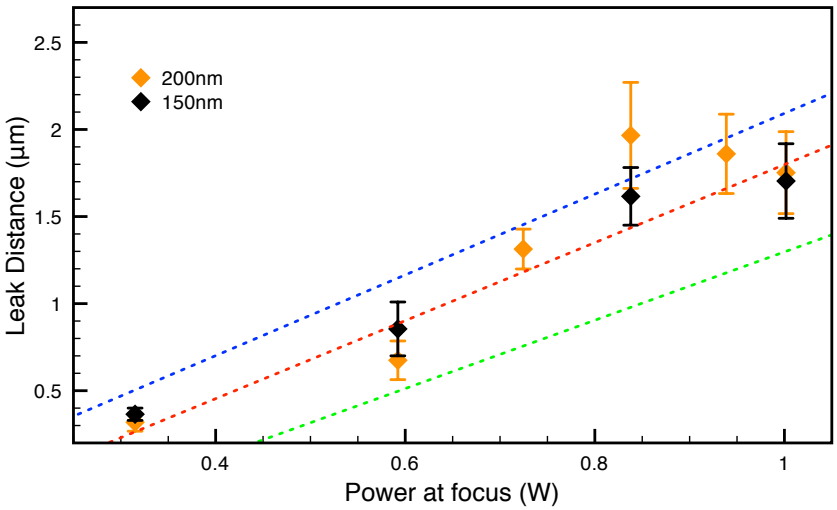

Figure 6.12: Leak distance for 150 and 200 nm gold particles at different laser powers. The lines are for comparison to the smaller particles, see figure 6.9.

6.2.2 Temperature increase for optically trapped gold particles

Both the critical phase transition distance from a trapped gold particle to membrane as well as the general sample temperature have been determined. By these direct experimental results and the Goldenberg model, the surface temperature of the particles can be deduced. The spot size for the trapping laser has been reported to be 1.8 μm.[31]. This was also confirmed by using the same experimental setup as in Bendix et al.[31] If the laser power in the sample is 1 W, the irradiance is given as

$$I = \frac{\text{Laser power}}{\text{Spot size area}} = \frac{1W}{\pi(d_{\text{spot}}/2)^2} \quad . \tag{6.6}$$

This mean flux is not strictly valid for a Gaussian beam profile, but it is an approximation near the trap focus. The irradiance and Mie absorption cross sections from chapter 2 can now be inserted into equation 6.2, giving a model for the heat increase for the gold particles. The model temperature increases for all sizes as functions of distance are plotted as the lines in figure 6.13.

The maximal surface temperature achievable at the highest laser power (1 W), can be determined by the data in figures 6.9 and 6.12 for all sizes. The irradiance at the trap focus and the experimentally found vesicle leakage-inducing distance can be inserted into equation 6.4.This estimate for A can then be utilized in equation 6.2 to yield the surface temperature for each size of gold particle.

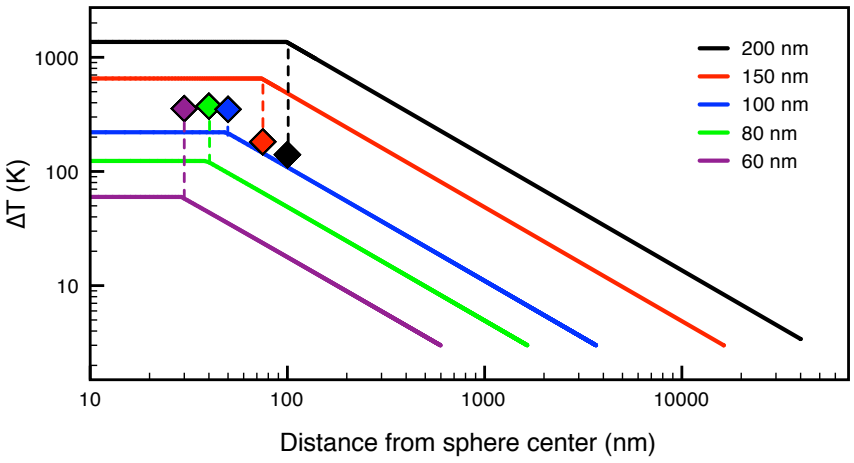

Figure 6.13: Model and experimental surface temperature increases as functions of distance, at a laser power of 1 W. Solid lines show the modeled surface temperature based on Mie theory. Squares represent surface temperatures for the gold particles, as determined via the Goldenberg relation. The dotted colored lines represent the aberration from the model expectation.

These surface temperatures determined by experiments are compared to the model prediction by the Mie absorption cross sections and the Goldenberg heat flow relation in figure 6.13. The experimentally found gold particle surface temperatures are shown as the square symbols, with the solid lines showing the model predictions for all distances from the particle center. If the model and the experimental values were exactly the same, the square symbols would align on the corner of each model line.

By regression via the Goldenberg relation, the determined surface temperatures at 1 W for the 60, 80, and 100 nm particles are: 355 ± 54^{o}K, 373 ± 35^{o}K, and 350 ± 67^{o}K. The derived surface ΔT for 150 nm at 1 W is 182 ± 23^{o}K and for 200 nm it is 140 ± 19^{o}K. For all values, the error margin listed is derived from the standard deviation in figures 6.9 and 6.12.

Block[43] (1990) is an often used citation that heating in water using optical tweezers effect a temperature increase of 1^{o}K/W, but this has been disputed in the recent years[44, 45, 46] with claims of up to 8^{o}K/W at the focus, stemming from absorption by water alone. The observations were based on trapped cells, liposomes as well as viscosity and the thermal motion of trapped polymer beads. For the data in this work, the control experiments mentioned on page 55 do not agree with the large heating of water near the focus reported by Peterman[46] assuming a sphere with the diameter of the trapping laser spot size. This model would mean reaching a phase-transition temperature at about one micron away from the trap focus, at a power of 1 W; this is not observed. As the original Block result of one degree increase near the focus is assumed to hold, this

would not raise the temperature beyond the stability of the stage thermal control setup - at least not for the leak distances measured.

Apart from the maximum laser power results, there is the direct relation of found leak distance to laser power from the previous section. For the linear fits seen in figure 6.9, there is a corresponding line describing the heat increase per watt of laser power. All data points for 60, 80, and 100 nm particles are used for the fitting, but for 150 and 200 nm only the points below 0.9 W are employed - to avoid the results at high laser powers, where there is a leveling off in the induced leak distances. This invalidates the direct comparison to data from the 60, 80, and 100 nm gold particles, but the relevancy is still present in the interest of trapping these larger particles in future assays. Using the linear fits as well as the data points in figure 6.9, the increase in surface temperature is shown in figure 6.14.

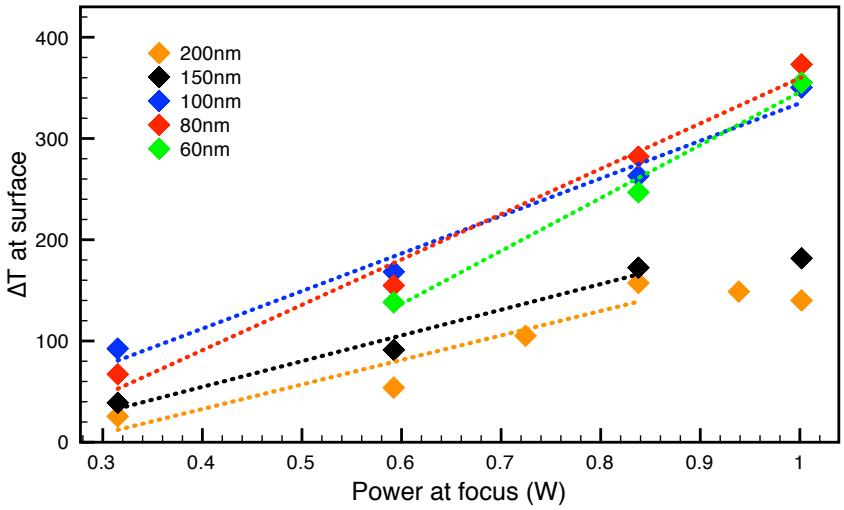

Figure 6.14: ΔT at the surface of each size of gold particle at the respective laser powers, as calculated for each data point available. The lines are fits to the determined surface temperature per input trapping laser power. For the 150 and 200 nm gold particles, the data fitted is cropped to maintain linearity.

It can be seen that there is a higher surface temperature produced for the smaller sizes, as detailed in table 6.1. A priori impression is that the inverse tendency should be prevalent - that the heat buildup should be stronger for the larger particles. The overall heat flow from each gold particle is dependent on the surface area: $A = 4\pi r^2$, so the heat flux for the 100 nm particles is still higher than for 60 and 80 nm, though they have approximately the same surface temperature at 1 W.

There are significant differences between the heating measured from gold nanoparticles trapped in 3D, as the heating decreases with particle size. In the 3D trapping assay

Table 6.1: Heat increase given by the slope of the linear fits of figure 6.14

Gold particle size	60 nm	80 nm	100 nm	150 nm	200 nm
K / W	523	448	371	254	242

the bead was allowed to move in the axial position to an equilibrium position where the scattering force exerted in the direction of the propagating laser light equated the gradient force exerted by the axially focussed laser beam.

The scattering cross section increases drastically with particle diameter as seen in chapter 2. Hence, in a 3D trapping assay one would expect the larger particles to be shifted further away from the trap focus in the axial direction than the smaller particles. This effect may explain the observed difference between trapping of the larger 150 and 200 nm particles sizes and the smaller sizes, because the intensity incident on the trapped particle is significantly smaller when the particle is displaced from the center of tight laser focus, and hence, the heating becomes smaller. If, on the other hand, the particle is forced to stay in the very center of the focus, as is the case for 2D trapping by Bendix[31], then the larger the particle, the larger the heating effect.

The information of the actual heating of a 3D trapped particle measured by the current method, together with a full Mie calculation could probably be used to estimate the displacement of the trapped nanoparticle with respect to the focus of the trap, a number long sought for in the optical trapping community. An early analysis for this scattering effect on the z-displacement of trapped particles is given in the following section.

6.2.3 Displacement in trap due to scattering

In chapter 2, it was established that the scattering cross sections for gold particles increase rapidly with size compared to the absorption cross sections, see figure 2.8 on page 13. For optical trapping, the total force on a particle can be split into two parts as seen in chapter 3, the scattering force which points in the axial direction and is directly dependent on the scattering cross section as

$$\mathbf{F_{sca}} = C_{\text{sca}} \frac{n_1 \langle \mathbf{S} \rangle}{c} \quad . \tag{6.7}$$

The gradient force was found in chapter 3 to depend on the polarizability of the particle as

$$\mathbf{F_{grad}} = \alpha \nabla \mathrm{E}^2 \quad . \tag{6.8}$$

Both forces are linearly related to the intensity of the optical trap and the ratio between them should be constant for different light intensities. Scattering cross sections and polarizabilities for gold particles of various sizes can be found by Mie theory, as shown in chapters 2 and 3.

As the scattering force increases with the scattering cross section, this may cause a displacement of the axial equilibrium position. This displacement is a function of both the scattering force, which pushes the particle along the axis; and the gradient force, which seeks to pull the particle toward the trap focus. An illustration of this proposed displacement is given in figure 6.15.

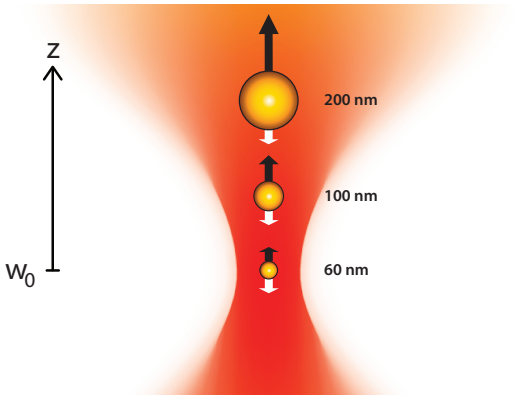

Figure 6.15: Illustration of proposed axial equilibrium positions for three different gold particle sizes, near the trap focus w_0. For each particle size, the displacement from the trap focus is dependent on the ratio between scattering force (black arrows) and gradient force (white arrows). The magnitude of the arrows shows the ratio between the two forces, but does not compare between sizes.

Let the ratio of the scattering cross section to the polarizability for gold particles be defined as

$$\beta(r) = \frac{C_{\mathrm{sca}}(r)}{\alpha(r)} \quad . \tag{6.9}$$

β is strongly size dependent, its absolute value is not of interest here, but the difference in magnitude between relevant gold particle sizes is interesting, since this allows an estimation of the z-displacement. If β is normalized to a value of 1 at a radius of 30 nm, the scaling between particle sizes is shown in figure 6.16. It is seen that β lies between 1 to 5 for 60, 80, and 100 nm gold particles; while up to 50 for 200 nm particles.

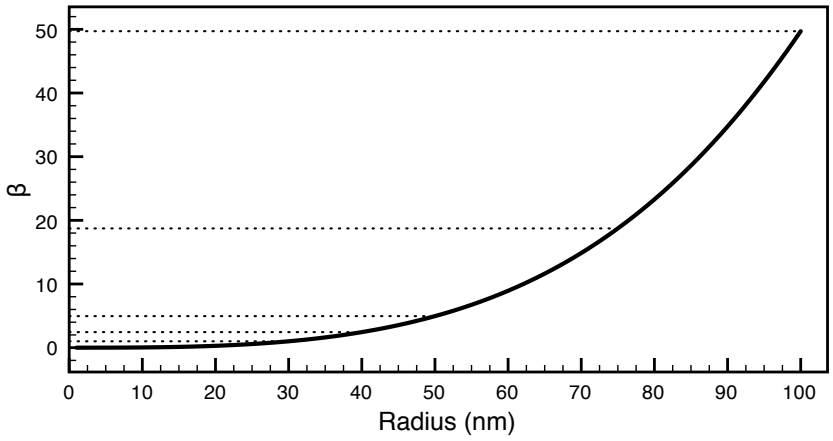

Figure 6.16: Scattering cross section to polarizability ratio, β, for a gold particle irradiated at 1064 nm wavelength for various sizes. Dotted lines indicate values for the gold particle sizes used in this thesis. Calculations were based on Mie results from chapter 2 and 3.

As evident from figure 6.16, the scattering force dominates the gradient force to a larger and larger extent as the particle size increases. Hence, the trapped particle is displaced further along the axial direction, the larger it is. A displacement from the trap focus lowers the intensity, due to the axial focus of the beam. Therefore, the temperature increase at a distance D from the center of a trapped gold nanoparticle is also dependent on the displacement, as it depends on the intensity I as

$$\Delta T_{\mathrm{out}}(D) = \frac{I C_{\mathrm{abs}}}{4\pi K_w D} \quad . \tag{6.10}$$

The surface temperatures for each size, as determined by the Goldenberg relation, can be re-interpreted if we assume that the actual intensity at their displacement is

$$I_{\text{ac.}} = \frac{I_{\text{focus}}}{\beta} \quad . \tag{6.11}$$

Here, it is assumed that 60 nm particles are trapped exactly at the trap focus. This way of estimating the actual intensity for each size is certainly only a working model, but the strengths of this simple analysis will be shown in the following.

To compare the temperature increase between the various sizes of gold particles as presented in figure 6.13 on page 57, let us do the following:

If the particle is displaced due to a large scattering force, the temperature at a distance D is given as

$$\Delta T_{\text{displaced}}(D) = \frac{I_{\text{ac.}} C_{\text{abs}}}{4\pi K_w D} \quad . \tag{6.12}$$

If, instead, the particle is at the focus, the temperature profile is given as

$$\Delta T_{\text{focus}}(D) = \frac{I_{\text{focus}} C_{\text{abs}}}{4\pi K_w D} \quad . \tag{6.13}$$

By the relation in equation 6.11, we have that

$$\Delta T_{\text{focus}}(D) = \beta \cdot \Delta T_{\text{displaced}}(D) \quad . \tag{6.14}$$

This is the equivalent of letting the proposed axial displacement of each particle size be cancelled, as shown in figure 6.17.

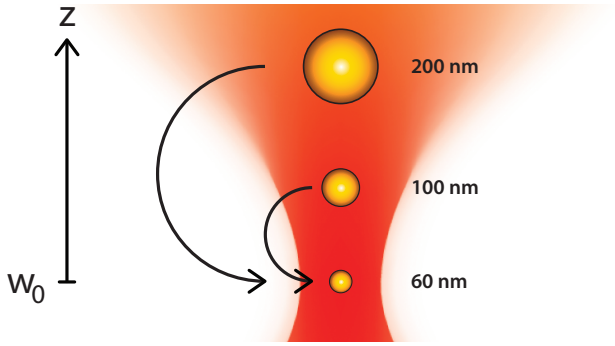

Figure 6.17: The temperature $\Delta T_{\text{focus}}(D)$ is found by equation 6.14. This corresponds to moving every size of particle to the trap focus.

In the Mie model, the intensity is assumed to be known. And in figure 6.13, this is chosen as the intensity at the focus. The experimentally measured temperature is $\Delta T_{\text{displaced}}(D)$, hence, if this should be compared to the Mie model, calculated using

I_{focus}, then $\Delta T_{\text{displaced}}(D)$ should be multiplied by β in order to get $\Delta T_{\text{focus}}(D)$. This have been done by using the β relation shown in figure 6.16 and normalizing it such that $\Delta T_{\text{focus}}(D) = \beta \cdot \Delta T_{\text{displaced}}(D)$ for a 60 nm particle. In other words, it is expected that the 60 nm particle is in the focus plane.

As shown in figure 6.18 it is apparent that by this simple analysis, the scaling between all gold particle sizes match very well with the model's expected ratios between gold particle sizes. There is now a much better agreement to the model expectations, particularly for 150 and 200 nm particles, on comparison to figure 6.13.

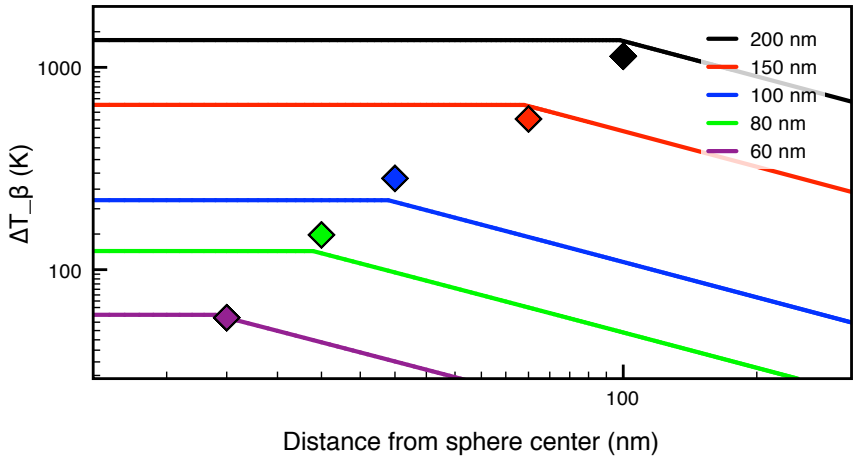

Figure 6.18: Full lines show the Mie theory prediction for the temperature profile around a trapped gold nanoparticle. Diamond symbols show the surface temperatures for all gold particle sizes at 1 W, factored by $\beta(r)$ and all values normalized by the same factor so that the found value for 60 nm gold particles (purple) is fixed at the temperature predicted by the heat increase model.

As the impact of β on actual displacement is not currently known, the act of fixing the 60 nm gold particle to the model for heat flow is valid in the sense that it predicts the differences in developed heat for the gold particles. The real physical displacement may be possible to determine experimentally, see outlook on page 68.

6.3 Discussion

In the preceding sections the results were outlined. Here, these findings will be compared to literature. The results from literature were obtained by a variety of experimental approaches, be that optical tweezers in 3D or 2D or broad illumination of fixed gold particles. The results for 1064 nm light interaction with particles will be focused on, with findings concerning other laser wavelengths also mentioned. Comparisons to work by other authors will be drawn in the annual order in which they appeared in print.

By observing the power spectrum for a 100 nm gold particle trapped in water, Seol et al.[47] lists a heating of $266^oK/W$. This is to be compared to the heating of $371^oK/W$ for 100 nm particles as presented in this thesis. Their model is based on the temperature dependency of Brownian motion, but as it is presented this does not accurately detect the surface temperature for the trapped particles - instead the average temperature of the volume the particle is allowed to sample by thermal motion is found. Removed just 20 nm from the particle, the temperature increase is 70% of that at the surface, as seen in figure 6.13, and so the heating efficiency may be under estimated. They make the assumption that the viscosity of water is constant in temperature, which is a mistake.

Urban et al.[48] made use of surface adsorbed vesicles, with 80 nm gold particles incorporated on the vesicle bilayer. The illumination of the particles was by a 532 nm Gaussian laser with an unfocused spot, which does not allow comparison to the present data. Further, having no control of position of the gold particles, in regard to the Gaussian beam combined with a non-uniform geometry of the very non-spherical vesicles displayed, leads to an introduction of unwanted parameters. On a side note, it was observed that the shriveled visual impression seen in Urbans vesicles was also evident in the vesicles presented in this thesis - but only at least 3+ hours after vesicle preparation. This was only observable for vesicles with a different solution inside their volume than outside, suggesting that there might be a refractive mismatch in Urbans vesicles. Any lensing effect from the vesicles could then disperse the irradiation laser, with a following loss of precision in the irradiation estimation.

Recent work in 2D optical trapping of gold particles attached on supported lipid bilayers by Bendix et al.[31] shows very comparative results, especially given that the very same experimental workbench was used as well as the gold particle production batches. The temperature measurements were based on the radial reach of the emerging fluidic phase of the bilayer from the particle, as visualized by lipid-fluorophore partitioning into or out of the fluidic domain. An advantage of this planar bound method is that the 1064 nm beam width at the particle is the same for all particle sizes - scattering can not result in a change in axial trapping depth, as the particle is surface confined to the bilayer. In their paper[31], they find that at high laser powers, the scattering from the laser causes the particles to blast off the surface into the solution. This indicates that the z-depth of irradiation does not correspond to a stable trapping depth for the 3D trapping in

this thesis, and so the irradiance is likely higher for their assay than for 3D trapping experiments conducted in solution.

In table 6.2 the values as reported by Bendix, Seol, and Mie theory are compared to the temperature increase found in this work.

Table 6.2: Comparison of determined surface temperature in K/W to the literature and Mie theory.

	60 nm	80 nm	100 nm	150 nm	200 nm
Present work	523	448	371	254	242
Bendix et al.		385	452	732	1640
Seol et al.			266		
Mie theory	60	124	220	652	1363

Heating by gold particles at a diameter of 100 nm may be underestimated in the work by Seol, and if the 2D trapping by Bendix has a higher irradiance due to a fixed surface, it is reasonable that the data for this work should fall between these two results.

The significant heat build up associated with the absorption of light by gold particles has been shown to cause steam bubble formation[49, 50]. This is thought by Saija[50] to be mainly a concern for the 150 and 200 nm gold particle sizes. They suggest that these sizes induce a small steam bubble layer, which in turn would affect trapping efficiency. The concept is consistent with the observation that the 3D trapping of these sizes exhibit similar leak distances as that of the 100 nm seen in figure 6.12 page 56, as well as the same trapping spring constants compared to the 100 nm size, as demonstrated by Bendix[24]. However, the simple model developed in section 6.2.3, suggests that it may instead be caused by a much higher displacement in the beam axis, thus lowering the irradiance.

Photo fragmentation or explosive fragmentation[8, 51] of the larger particles could entail a violent destruction of the trapped particles, but the data would not be expected to have a standard deviation comparable in magnitude to that of the smaller gold particles, given that the resulting size distribution after fragmentation is assumed to be very broad. This would lead to large deviations for the leak distances determined, and this is not seen in the data.

Chapter 7

Conclusion

The purpose of this project was to directly measure the heating of 3D optically trapped gold nanoparticles due to the irradiation of the 1064 nm trapping laser, by exploiting the permeability of lipid bilayers at their phase transition temperature.

Designing the experiment to use giant unilammelar vesicles tethered through the avidin-biotin bridging on to a supported lipid bilayer succeeded in establishing a reproducible working setup. By having the trapped particle in the heat conductively homogeneous medium of a water solution, the distance at which point the vesicle became leaky was detected and could be used to determine the surface temperature at the gold particle, using the Goldenberg relation. The lipid phase transition was an event with two indicators which were experimentally observable: the leakage of fluorescent dye Alexa Hydrazide 488, caused by the permeability of the membrane at the phase transition; and a local partitioning of bilayer incorporated Texas Red-DHPE lipid into the induced fluidic part of the vesicle.

The model was constructed by the Mie theory derived absorption cross sections and the flow of heat from a sphere, as described by the Goldenberg relation.

Maximally found surface temperatures for trapped gold particles at 1 W laser power are; 355±54^{o}K for 60 nm, 373±35^{o}K for 80 nm, 350±67^{o}K for 100 nm, 182±23^{o}K for the 150 nm size and 140±19^{o}K for 200 nm. The lower surface temperatures for the 150 and 200 nm gold particles are probably an effect of the increased scattering force they are subject to compared to the sub 100 nm particles.

For each particle size the heat increase was found to be 523^{o}K/W for 60 nm, 448^{o}K/W for 80 nm, 371^{o}K/W for 100 nm. 80 and 100 nm gold particle results compare well with the results reported in literature, while no literature data is available for the size of 60 nm. For the two remaining sizes, the linear scaling up to 0.85 W was characterized to be 254^{o}K/W for 150 nm and 242^{o}K/W for the 200 nm particles.

Mie theory was used to calculate the optical cross sections for each size, and by intro-

ducing a ratio of scattering cross section to polarizability as a rough estimate of the axial displacement of trapped particles is gained. This factor for the irradiation at the beam width of the trapped particles can accurately describe the recorded scaling in heat developed for all sizes of gold particles considered in this thesis, in comparison to the model predictions.

The markedly less efficient trapping of the large 150 and 200 nm particles is proposed to be related to the much larger scattering cross section in comparison to their dipole polarizability for these sizes, in respect to the 60, 80, and 100 nm gold particles.

To conclude, it was possible to accurately establish the surface temperature of fully trapped gold nanoparticles at a wide range of laser powers. This was accomplished by employing a reversible and controlled release of vesicles carrying a fluorescent dye.

The main conclusions of this thesis are also given in the appendix on page 77, which is the scientific paper aimed for *JACS* written on the basis of my results.

7.1 Outlook

Owing to their large absorption cross sections across the visual spectrum as well the near infrared, the general expectations of using irradiated gold nanoparticles as local heat generators in industrial applications[5] and medicinal therapies[1, 52, 53] seem well founded. Research in lipid bilayer phase interfaces may benefit from the ability to induce fast local state transitions, with a sharp well defined interface boundary as seen in the plane[31].

Targeted drug delivery or direct ablation of cells are also very real possible uses for gold nanoparticles, with their highly local and size dependent heating, as detailed in chapter 1.

It may be possible to use the gold particles as a research tool to observe single molecule events, by the few nanosecond equilibration of heat near the gold particles. For example, a ribosome complex may be turned on and off by a fast switching in and out of its thermodynamic working window.

Further projects may consider the expansion of individual layers of multi lamellar vesicles, as seen in movie-file SI6. Layers bud off from the stacked layers with isolated layers individually visually resolved, something that could be of interest in inter-membrane research.

Future work may entail an experimental determination of the possible trap displacement, as introduced in section 6.2.3. This may be accomplished by the setup described in this thesis, by utilizing that the depth of the confocal microscopy plane and the trap focus depth can be locked together. Then by keeping a gold particle in optimal confocal focus, the confocal plane exactly contains the equilibrium displacement position in the trap for

the given size of particle. By letting the gold particle escape the trap and shifting the confocal focus in the z-depth(and trap by the same amount) until a fluorophore covered surface is optical focus, the trap spot can be extracted by the area it bleaches. This may then give the z-displacement as shown in figure 7.1.

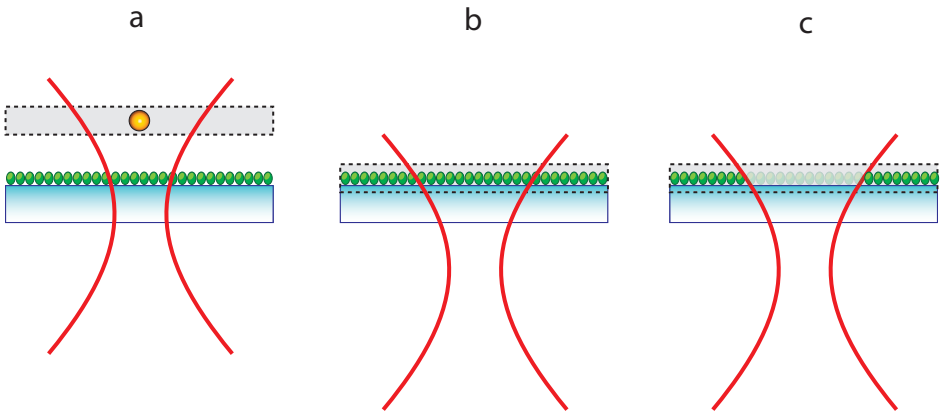

Figure 7.1: Equilibrium axial displacement position determination for an optically trapped gold particle. Trap profile is shown in red lines. a) A gold particle is trapped in solution, while confocally imaged with the confocal focal plane indicated by the grey dotted box. b) The particle is removed and the confocal focus is shifted onto a fluorophore covered surface (green dots). The trap is locked to the confocal depth change and is thus shifted by the same amount. c) By observing the bleaching spot of the trapping laser, the z-displacement position of optically trapped gold particles can be obtained.

Chapter 8

Appendices

8.1 Appendix 1 - Matlab scripts

The script code for solving Mie theory for gold particles of an arbitrary size follows. It can also be found as a file on the attached CD.

mie.m is the main generator of optical cross sections and can be polled by external scripts inputting a given radius. For testing purposes, *mie_vis.m* can be used to execute mie.m and display an optical spectrum.

8.1.1 Main Mie solution script - mie.m

```
function [Q_ext,Q_sca,Q_abs,C_ext,C_sca,C_abs,wavelength_i] = mie(r)
%Function to calc. mie coef's based on the macro optical properties of
%mediums.

%Common constants:
%Plancks in eV*s:
h = 4.13566733e-15;
%Speed of light in m/s:
c = 3e8;

%Initial constants for gold and water from:
%Johnson and Christy. Optical constants of the noble metals.%Physical
%Review B (1972)
%and
%Hale and Querry. Optical constants of water in the 200-nm to 200- m
%wavelength region. Applied Optics (1973) vol. 12 (3) pp. 555-563
n_gold = [0.92 0.56 0.43 0.35 0.27 0.22 0.17 0.16 0.14 0.13 0.14 0.21 ...
          0.29 0.43 0.62 1.04 1.31 1.38 1.45 1.46 1.47 1.46 1.48 1.50 ...
          1.48 1.48 1.54 1.53 1.53 1.49 1.47 1.43 1.38 1.35 1.33 1.33 ...
          1.32 1.32 1.30 1.31 1.30 1.30 1.30 1.30 1.33 1.33 1.34 1.32 ...
```

```
          1.28];

k_gold = [13.78 11.21 9.529 8.145 7.150 6.350 5.663 5.083 4.542 4.103 ...
          3.697 3.272 2.863 2.455 2.081 1.833 1.849 1.914 1.948 1.958 ...
          1.952 1.933 1.895 1.866 1.871 1.883 1.898 1.893 1.889 1.878 ...
          1.869 1.847 1.803 1.749 1.688 1.631 1.577 1.536 1.497 1.460 ...
          1.427 1.387 1.350 1.304 1.277 1.251 1.226 1.203 1.188];

%Water chosen closest to element from johnson et al.:
n_water = [1.306 1.317 1.321 1.324 1.327 1.327 1.328 1.329 1.330 1.331 ...
           1.331 1.332 1.333 1.333 1.334 1.335 1.336 1.337 1.338 1.339 ...
           1.339 1.341 1.341 1.343 1.343 1.346 1.346 1.349 1.349 1.349 ...
           1.354 1.354 1.354 1.362 1.362 1.362 1.362 1.373 1.373 1.373 ...
           1.373 1.373 1.396 1.396 1.396 1.396 1.396 1.396 1.396];

%Photon energy at the values supplied above (in eV):
e_gold = [0.64 0.77 0.89 1.02 1.14 1.26 1.39 1.51 1.64 1.76 1.88 2.01 ...
          2.13 2.26 2.38 2.50 2.63 2.75 2.88 3.00 3.12 3.25 3.37 3.50 ...
          3.62 3.74 3.87 3.99 4.12 4.24 4.36 4.49 4.61 4.74 4.86 4.98 ...
          5.11 5.23 5.36 5.48 5.60 5.73 5.85 5.98 6.10 6.22 6.35 6.47 ...
          6.60];

%Generation of wavelength-table from e_gold:
wavelength = h*c./e_gold;

%Interpolation of optical constants, speed is not an issue...
e_gold_i = e_gold(1,1):0.02:e_gold(1,49);
wavelength_i = h*c./e_gold_i;
n_gold_i = interp1(wavelength,n_gold,wavelength_i,'cubic');
k_gold_i = interp1(wavelength,k_gold,wavelength_i,'cubic');
n_water_i = interp1(wavelength,n_water,wavelength_i,'cubic');

%Generation of relative refractive index (for mie) at a given wavelength:
m = (n_gold_i+1i*k_gold_i)./n_water_i;

%Size-factor x, wavelength relative to medium:
x = (2*pi*r)./(wavelength_i./n_water_i);

%Calculation of Mie coefficients a_n, b_n, c_n and d_n, as per bohren and
%huffman
%Further note: Kreibig is incomplete in comp. to bohren+huffman
%Further we set the magnetic permeability ratio to unity, simplifying the
%coefficients..
%Spherical besselj fct. can be found from normal Bessel fct by:
%SB_n(z) = sqrt(pi/(2*z))*J_(n+(1/2))(z)

%nstop calced as recommended by B+H p477:
xl = x(1,size(x,2));
nstop = round(xl+4*xl^(1/3)+2);

%Preallocation
C_ext_loop(nstop,size(e_gold_i,2)) = 0;
C_sca_loop(nstop,size(e_gold_i,2)) = 0;
```

```
for n = 1:nstop
jx(n,:) = besselj(n+1/2,x).*sqrt(pi./(2.*x));
jmx(n,:) = besselj(n+1/2,m.*x).*sqrt(pi./(2.*(m.*x)));
yx(n,:) = bessely(n+1/2,x).*sqrt(pi./(2.*x));
hx(n,:) = jx(n,:)+1i.*yx(n,:);

an(n,:) = ( (m.*m.*jmx(n,:).*gradient(x.*jx(n,:),x)) ...
          - ...
          (jx(n,:).*gradient(m.*x.*jmx(n,:),m.*x)) ) ...
          ./ ...
          ( (m.*m.*jmx(n,:).*gradient(x.*hx(n,:),x)) ...
          - ...
          (hx(n,:).*gradient(m.*x.*jmx(n,:),m.*x)) );

bn(n,:) = ( (jmx(n,:).*gradient(x.*jx(n,:),x)) ...
          - ...
          (jx(n,:).*gradient(m.*x.*jmx(n,:),m.*x)) ) ...
          ./ ...
          ( (jmx(n,:).*gradient(x.*hx(n,:),x)) ...
          - ...
          (hx(n,:).*gradient(m.*x.*jmx(n,:),m.*x)) );

%Optical coefficients, note to self: matlab comd. "abs" is mod of a complex
%number.
C_ext_loop(n,:) = (2*pi)./((x./r).^2).*(2*n+1).*real(an(n,:)+bn(n,:));
C_sca_loop(n,:) = (2*pi)./((x./r).^2).*(2*n+1).*(abs(an(n,:)).^2 ...
                  + abs(bn(n,:)).^2);
end

%Final sums:
C_ext = sum(C_ext_loop,1);
C_sca = sum(C_sca_loop,1);
C_abs = C_ext - C_sca;

%Extinction-efficiencies calculated from scatter cross-sections
Q_ext = C_ext./(pi*r^2);
Q_sca = C_sca./(pi*r^2);
Q_abs = C_abs./(pi*r^2);
```

8.1.2 Mie spectra for a single radius - mie_vis.m

```
function mie_vis
%Input section:
%Radius in m
r = 100e-9;
%Calling mie.m
[Q_ext,Q_sca,Q_abs,C_ext,C_sca,C_abs,wavelength_i] = mie(r);

%Output section:
%Final output figure
figure(100)
plot(wavelength_i*1e9,Q_ext,'+',wavelength_i*1e9,Q_abs,'+', ...
     wavelength_i*1e9,Q_sca,'+')

save mie_vis_save.mat
```

8.2 Appendix 2 - Fluorescent excitation spectra

Fluorescence excitation spectra consists of two spectra overlaid into a final figure. First, the spectrum for excitation of a singlet state for a fluorophore is shown at lower wavelength, see the blue line in figure 8.1. The emission spectrum as a results of singlet state decay is then seen at higher wavelength, as the red line in figure 8.1.

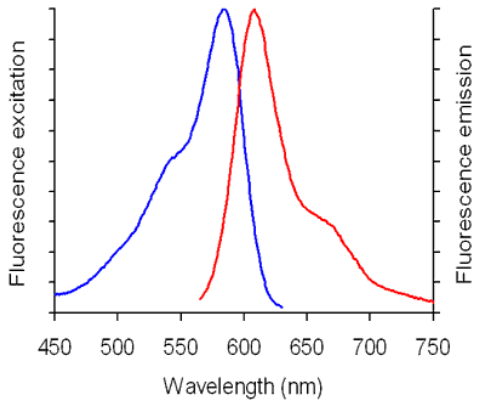

Figure 8.1: Texas Red-DHPE Spectrum

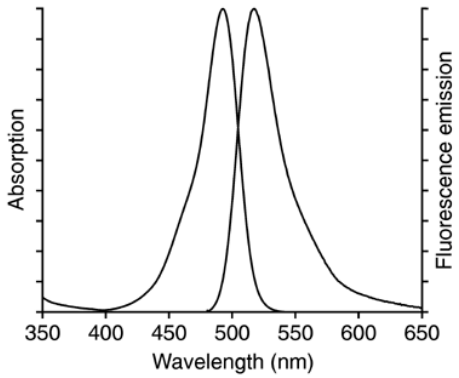

Figure 8.2: Alexa Hydrazide 488 Spectrum

8.3 Appendix 3 - Intensity plots from experiments

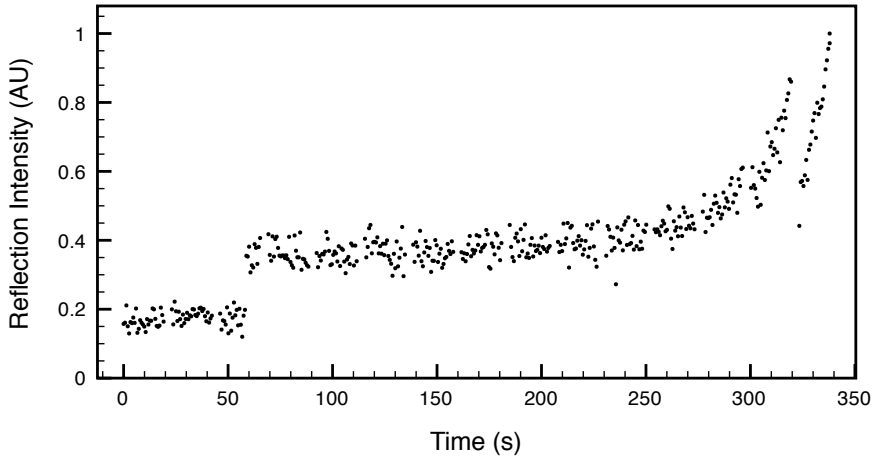

Figure 8.3: Reflected light from a trapped gold particle, note the sudden incursion by a second particle at 60 s.

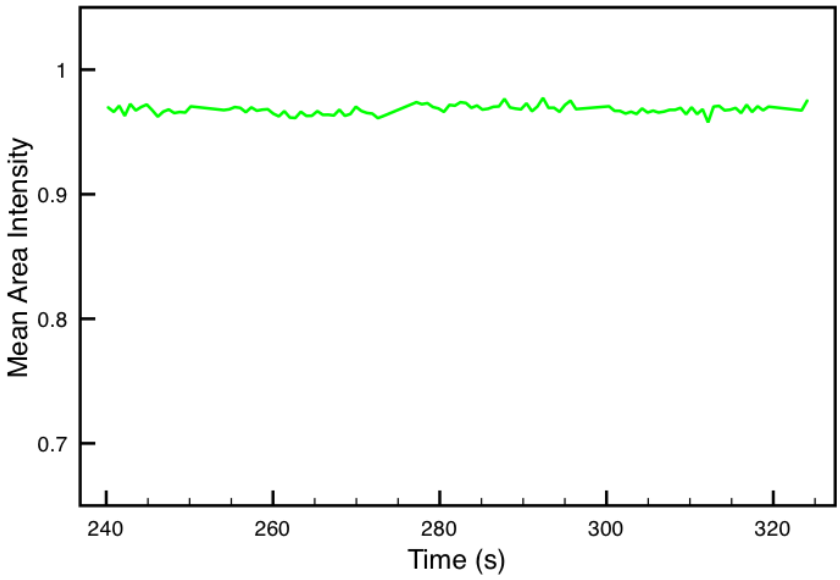

Figure 8.4: Intensity profile for the Alexa dye of moviefile *SI5*, trapping a gold particle inside a vesicle to show no heat-inactivation of Alexa.

Chapter 9

Articles

The following paper is preprint and due to be submitted to JACS shortly.

Controlled vesicle release by optically trapped gold nanoparticles

Anders Kyrsting, Poul M. Bendix, Dimitrios Stamou, and Lene B. Oddershede*
Niels Bohr Institute, University of Copenhagen, Denmark
Received July 5, 2010; E-mail: oddershede@nbi.dk

Irradiation of a metallic nano particle results in excitation of plasmon resonances giving rise to a significant heating of the metallic nanoparticle. This effect can be advantageously used in biomedical contexts, e.g., for photothermal cancer therapy.[1,2] This effect has been utilized to quantify the temperature profile around a metallic nanoparticle embedded in a two-dimensional lipid bilayer[4] and for making phospholipid membranes undergo phasetransitions.[3] Heated gold nanoparticles have potential to mediate release of polymer micro-capsules and hardened lipid vesicles.[6–9] Here we show how to use a gold nanoparticle optically trapped in three dimensions to perform a controlled cargo release of giant unilammelar vesicles, this mechanism having potential for controlled drug delivery assays. In addition, the results for the first time quantify the temperature profile surrounding a metallic nanoparticle optically trapped in three dimensions and reveals that the scattering force causes the beads center to be significantly dislocated from the trap center.

Due to their large absorption, individual metallic nanoparticles in aqueous suspensions are readily trapped by a strongly focused infra red laser beam, an optical trap.[10–14] In the present experiments, gold nanoparticles with diameters in the range of 60-200nm were optically trapped. The optical trap was based on a Spectra Physics J201-BL-106C 1064 nm laser beam and implemented in a Leica SP5 confocal microscope, the experimental settings are in detail described in[4] and in the supporting information. Gold nanoparticles were kept in a suspension which also encompassed surface tethered giant unilammelar vesicles with diameters around 10 μm. The GUVs contained the Alexa Hydrazide fluorophore (AH)with emission wavelength 517 nm. At temperatures below the phase transition the membrane is impermeable to this fluorophore, at the phase transition temperature the membrane becomes permeable to the fluorophore[15] and the cargo of the GUV will leak out. The vesicles constituted primarily of $DC_{15}PC$ lipids with a phase transition temperature of 33°C, these lipids were enriched with 3% Texas Red-PE fluorophore, emission at 601 nm, for easy visualization of the membrane and with 0.1% Biotin-PE for tethering the GUV to an avidin containing Supported Lipid Bilayer surface. The sample chamber was kept at (8 ± 0.5)°K below the lipid phase transition temperature, the experimental settings are detailed in supplementary information. The experiment was conducted by moving an optically trapped gold nanoparticle towards a supported GUV at a constant speed of 0.01μm/s using a piezo electrical stage with capacitative feedback (PI-P5173CL). The Alexa Hydrazide inside the GUV, the Texas Red marked GUV, as well as the optically trapped gold nanoparticle were visualized by confocal microscopy, pictures were constantly taken at 1.28 frames/sec, hence, the bead had moved 7.8 nm with respect to the supported GUV between two consecutive frames.

At a critical distance between the optically trapped gold nanoparticle and the surface of the GUV, the GUV became leaky and the AH escaped from the GUV lumen by diffusion through the membrane. This is visualized in Figure 1a, which shows three snapshots during an experiment. The AH inside the GUV is green, the GUV membrane red, and the trapped gold nanoparticle appears as a bright white spot. In Fig. 1a part I the trapped bead is far away from

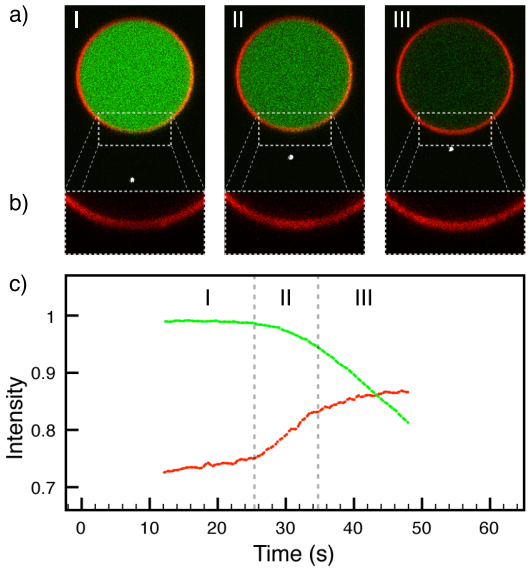

Figure 1. Controlled leakage of a GUV upon approach of an optically trapped gold nanoparticle. (a) Confocal images of a GUV surface (red), its cargo (green), and an optically trapped gold nanoparticle (bright white spot) as the trapped nanoparticle approaches the GUV. (b) Zoom in on the membrane in the boxes of (a). (c) Intensity of the flourophores in the boxed regions of (a) as a function of time, the AH signal is normalized by its initial value, the intensity of Texas Red is normalized by the initial AH value. The GUV becomes leaky around t = 26 s. .

the GUV and the content of the GUV is intact, in part II the trapped bead is closer to the membrane, AH is leaking out and the intensity of AH in the lumen has decreased, and in part III the trapped bead is even closer to the GUV and the interior of the GUV has almost completely leaked out. Care was taken to have the optically trapped bead in the same axial height as the equator of the GUV. Fig. 1b shows zoom-ins on the Texas Red emission in the boxed region of Fig. 1a, hence, it is a zoom in on the membrane part closest to the optically trapped nanoparticle. The Texas Red labeled lipids preferably localized in the fluid region, hence, the increase of fluorescense in the region closest to the optically trapped gold nanoparticle during its approach is due to a local melting of the membrane. Also, it is clear that the membrane did not rupture during the phase transition or while in the lipid phase. Fig. 1c quantifies the total intensity of the AH and of the Texas Red as a function of time within the boxed region shown in Fig. 1a. Until approximately 26 s have elapsed there was essentially no change in the AH emission, bleaching was negligible. Then AH started to leak and the lumen intensity decreased in a nearly linear fashion. Simultaneously, the intensity of Texas Red in the membrane region constantly increased. We defined the critical leaking distance as the distance between the trapped gold nanoparticle and the surface of the GUV at the time where a linear fit to the decrease in AH fluorescence intersects with the horizontal line defining the non-leaked

AH intensity.

The critical leaking distances were determined for a variety of laser powers and particle diameters (60, 80, 100, 150 and 200 nm), the results are shown in Figure 2. Each point is an average of 5 independent experiments (different particles), the error bars denote one standard deviation. As the gold nanoparticle is located at a distance from any surface which is several orders of magnitude larger then its diameter, the heat profile surrounding it is well described by the Goldenberg relation:[16]

$$\Delta T(D) = \frac{AR^3}{3K_w D}. \quad (1)$$

Here, A is heat input per volume unit, K_w is the thermal conductivity of water, D is the distance from the center of the sphere, and R is the radius of the heated sphere. $A = IC/V$, where I is the intensity of the laser power, C is the absorption cross section, which for these particle sizes is correctly calculated using Mie theory, and V is the particle volume. Hence, for a $\Delta T(D)$ corresponding to the difference between the ambient temperature and the phase transition temperature, equation 1 predicts a linear relationship between the leak distance, D and the laser power I. This is verified for several particle sized in Figure Figure 2 where the dashed lines are linear fits to the data points. For the two largest particle sizes the relation between leak distance and power is only increasing up to laser powers up to ~ 0.9W, at higher laser powers D decreases and eq. 1 is not obeyed, these data points are not included in the linear fit (dashed black and orange lines). The reason for this discrepancy is probably because a significant scattering force acting on these large particles at high laser powers, thus causing a significant displacement of the particle from the trapping focus. Interestingly, these two larger particle sizes have also been reported to have significantly different scaling properties of the spring constant, characterizing the strength of their interaction with the electromagnetic field than the smaller particles.[11,14]

Using equation 1 the temperature at the surface, $\Delta T(D)$, of the nanoparticle as a function of I can be calculated, this is shown for the five particle sizes in supplementary figure S1. The slopes of $\Delta T(D)$ versus I can be used to find the heating at the surface of the particles, $\Delta T(D)/I$. We find these values to be $523°K/W$ for the 60 nm particle, $448°K/W$ for 80 nm, and $371°K/W$ for 100 nm, $253°K/W$ for 150 nm, and $242°K/W$ for 200 nm, respectively. To our knowledge, these are the first direct measurements of heating associated with a metallic particle optically trapped in 3D. The heating associated with a gold nanoparticle which is embedded in a lipid bilayer and optically trapped in 2D reported in Ref.[4] is $385°K/W$ for 80 nm, $452°K/W$ for 100 nm, $732°K/W$ for 150 nm, and $1640°K/W$ for 200 nm, respectively. In[5] a more indirect method as used to measure the heating around a 3D trapped 100 nm gold nanoparticle, they found a heating of $266°K/W$.

There are significant differences between the heating measured from gold nanoparticles trapped in 2D and in 3D: For all particles above 80 nm the heating measured from a 2D trapped gold nanoparticle is larger than when the nanoparticle is trapped in 3D and hence free to move (within the trap) in the axial direction. In addition, during 3D trapping the heating decreases with particle size, whereas the heating increases with particle size during 2D trapping. In the 2D trapping assay the distance between the laser focus and the position of the particle was constant as the trap was always positioned as accurately as possible with its center at the bead, the bead being confined in the axial direction by the lipid bilayer. In the 3D trapping assay the bead was allowed to move in the axial position to an equilibrium position where the scattering force exerted in the direction of the propagating laser light equated the gradient force exerted by the axially focussed laser beam.[?] The larger the scattering force with respect to the gradient force, the further away from the trap center this new equilibrium position is located. The scattering force increases drastically with particle diameter (see supplementary figure 2), hence, in a 3D trapping assay one would expect the larger particles to be shifted further away from the trap focus in the axial direction than the smaller particles. This effect explains the observed difference between 2D and 3D trapping, because the intensity incident on the trapped particle is significantly smaller when the particle is displaced from the center of tight laser focus, and hence, the heating becomes smaller. If, on the other hand, the particle is forced to stay in the very center of the focus, as is the case for 2D trapping, then the larger the particle, the larger the heating effect. In fact, the information of the actual heating of a 3D trapped particle measured by the current method, together with a full Mie calculation could probably be used to estimate the displacement of the trapped nanoparticle with respect to the focus of the trap, a number long sought for in the optical trapping community.

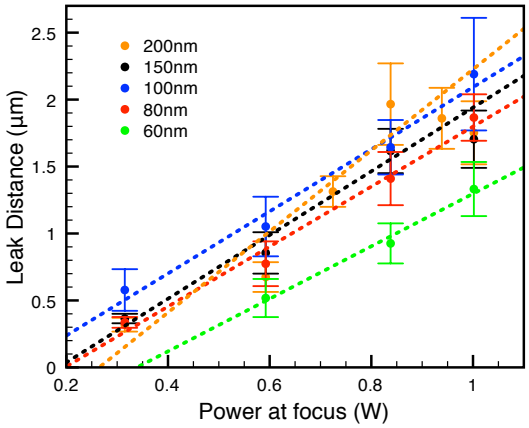

Figure 2. Leak distance, D, as a function of laser intensity at the sample for gold nanoparticles with diameters 60, 80, 100, 150, and 200 nm. Dashed lines are linear fits to the data points for each particle size.

We presented a novel nano-assay for a controlled release of vesicle cargo. Due to absorption of laser light an optically trapped gold nanoparticle starts to irradiate heat which then causes the temperature of the vesicle to increase to the phase transition temperature, at which it becomes leaky and the cargo spills out. This is accompanied by a local melting of the vesicle membrane. In addition, our method serves as a way to quantify the heating profile surrounding a gold nanoparticle trapped in three dimensions. Due to the scattering force, the trapped bead is located significantly above the focus point of the optical trap, this giving rise to a different relations between particle radius and the resulting heat profile for a 3D trapped particle than for a 2D trapped particle. We envision this technique will become useful for nano-bio-medicine delivery assays, where an external laser will trigger the release and/or a quantified local ablation of biological specimen.

Acknowledgement We acknowledge fruitful discussions with S.N.S. Reihani. LBO acknowledges financial support from the University of Copenhagen Excellence grant.

Supporting Information Available: Full experimental procedure. Supplementary figure 1: surface temperature as function of laser power. Supplementary figure 2: Extinction coefficient as function of particle size and laser wavelength. Supplementary figure 3: Bleaching of cargo as a function of time. Video: Typical experiment.

References

(1) Numata, T.; Tatsuta, H.; Morita, Y. *IEEJ Transactions on ...* **2007**.

(2) El-Sayed, I.; Huang, X.; El-Sayed, M. *Cancer letters* **2006**.
(3) Urban, A.; Fedoruk, M.; Horton, M.; Rädler, J. O. *Nano Letters* **2009**.
(4) Bendix, P.; Reihani, S.; Oddershede, L. *ACS nano* **2010**.
(5) Seol, Y.; Carpenter, A.; Perkins, T. *Optics letters* **2006**.
(6) Needham, D.; Dewhirst, M. *Advanced drug delivery reviews* **2001**, *53*, 285–305.
(7) Pissuwan, D.; Valenzuela, S.; Cortie, M. *TRENDS in Biotechnology* **2006**, *24*, 62–67.
(8) Pitsillides, C.; Joe, E.; Wei, X.; Anderson, R.; Lin, C. *Biophysical Journal* **2003**, *84*, 4023–4032.
(9) Angelatos, A.; Radt, B.; Caruso, F. *J. Phys. Chem. B* **2005**, *109*, 3071–3076.
(10) Svoboda, K.; Block, S. *Optics letters* **1994**.
(11) Hansen, P.; Bhatia, V.; Harrit, N.; Oddershede, L. *Nano Letters* **2005**, *5*, 1937–1942.
(12) Selhuber-Unkel, C.; Zins, I.; Schubert, O.; SoÌÂĹnnichsen, C.; et al., *Nano Letters* **2008**.
(13) Bosanac, L.; Aabo, T.; Bendix, P.; Oddershede, L. *Nano Letters* **2008**, *8*, 1486–1491.
(14) Hajizadeh, F.; Reihani, N. *Opt. Express* **2010**.
(15) Blicher, A.; Wodzinska, K.; Fidorra, M. *Biophysical Journal* **2009**.
(16) Goldenberg, H.; Tranter, C. *British Journal of Applied Physics* **1952**, *3*, 296–298.

TOC illustration

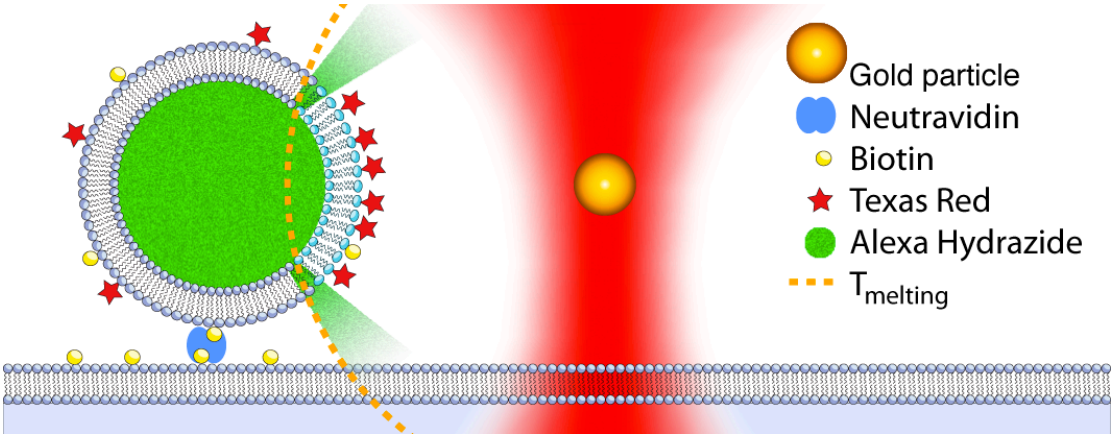

Methods and Materials

0.14 μm thickness cover glasses were rinsed by immersing them into piranha solution for 30 min and flushing with Millipore water 5 times. The sample chamber which fitted into our heating device (Harvard systems) consisted of a Ø25 mm cover glass with a Teflon ring on top. Between these two a rubber ring is placed to provide a seal. The stack is then compressed by an aluminum housing.

POPC (#770557) and Biotinyl PE (#870277) lipids from Avanti Polar Lipids were mixed in chloroform each at a concentration of 25 mg/ml (100:1). 400 ml solution was evaporated in a 5 ml glass vial and placed for two hours in a vacuum desiccator. Lipids were then rehydrated in 0.1 M PBS overnight and extruded 9 times at a filter pore-size of 100 nm. PBS solution was made from PBS tablets from Invitrogen (#18912-014) in 700mL Millipore water. This stock was used to form supported lipid bilayers in the sample chambers by adding 200 μl lipid suspension on the glass cover and leaving it to settle overnight. The sample chambers were rinsed by flushing10 times with Millipore water followed by 5 times with 0.1 M PBS. Neutravidin was added to a concentration of 0.02 M and allowed to settle for 5 min and then washed 5 times with 0.1 M PBS.

Giant Unilamellar Vesicles (GUVs) were produced using DC15PC (#850350), Biotinyl PE (#870277) both from Avanti Polar Lipids, and Texas Red conjugated PE (#T1395MP) from Invitrogen. They were mixed at the ratios 1000:1:30 in chloroform. The solution was dripped into a custom made Teflon cylindrical container and allowed to evaporate, followed by 2 hours in a vacuum desiccator. 5 ml of 0.2 M D-Sorbitol was added at 37°C and the container was kept at 37°C for 3 hours, with gentle shaking every 30 min. The suspension was allowed to cool to room temperature and transferred to vials using a pipette with an opening of Ø3 mm.

Alexa 488 Hydrazide (#A-10436) from Invitrogen was added, to each sample we added 8 μl 10mg/ml. 2 μl 0.5 M NaCl solution was added to this solution.

To fill the GUVs with the fluorophore, ~10 μl GUV suspension was added. This final solution was heat-cycled past the phase transition temperature of the GUV main lipid by leaving it in a 37 C incubator for 10 min and at 24 C for 5 min, the procedure was repeated 3 times.

The filled GUVs were transferred to the prepared sample chamber immediately after the heat cycle process and left to settle for 30 min. Excess Alexa Hydrazide was washed away very gently using 0.1 M PBS.

Gold Nano Particles (GNP) were prepared by sonicating 450 μl from each stock solution by British Biocell International. 50 μl thiolated PEG from Aldrich Sigma at 5 mg/ml was added to each suspension and agitated at 1000 rpm for 30 min. The samples were then spun down and the supernatant aspirated. The particles were resuspended in 500 μl Millipore water.

Samples were imaged using a Leica SP5 confocal microscope. An optical trap based on a 1064nm Nd : YVO4, 5 W laser (Spectra Physics J201-BL-106C) was implemented in the microscope. AH 488 was excited at 488nm and imaged in fluorescence-mode in the range 495-565nm. Texas Red DHPE was excited at 594nm and imaged at 610-710nm. The gold nanoparticles were imaged using backscattered light from the 594nm source, in the range 589-599nm. All images were collected simultaneously.

A Leica PL APO NA:1.2 100x water immersion objective was used for all experiments.

Supporting figure 1:

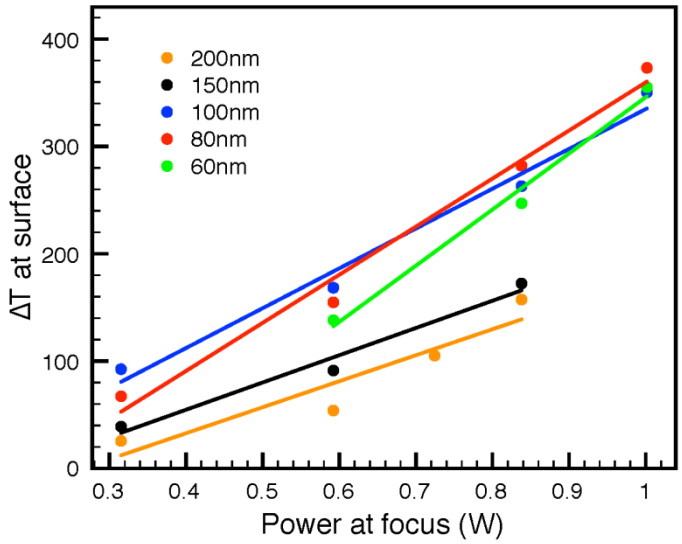

Surface temperature of trapped nanoparticle as a function of laser power for five different particle sizes. The filled circles are the values calculated via equation 1 from the values of leak distance versus laser power

given in Figure 1 for each particle size. The filled lines are the values corresponding the the dashed lines in figure 1.

Supplementary figure 2:

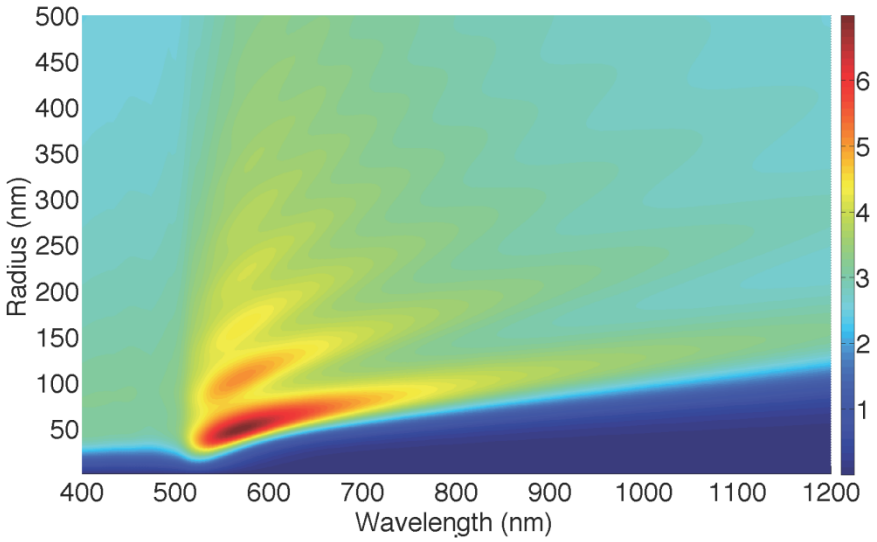

Extinction coefficient as function of particle size and laser wavelength. Red denotes large value, blue denotes small value. The scattering force is directly proportional to the extinction coefficient, hence, it is strongly dependent on particle size. The larger the particle, the larger the extinction coefficient.

Supplementary figure 4:

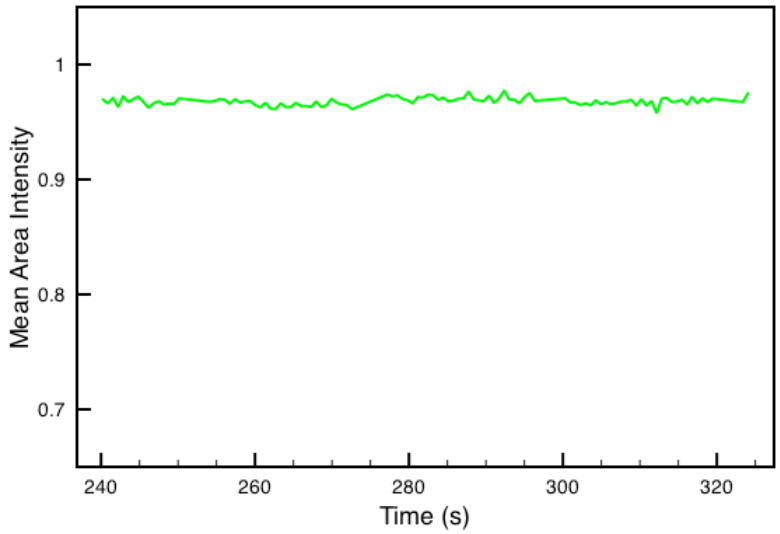

Bleaching of GUV cargo. The graph shows the intensity emitted from the cargo as a function of time. During the experiment, a gold nanoparticle is

trapped in the center of the GUV, but far enough from the GUV membrane to make it permeable. No bleaching is observable, the timescale of this control experiment by far exceeds the timescale of a typical experiment (compare to Figure 1).

Bibliography

[1] D. Pissuwan, S. Valenzuela, and M. Cortie, "Therapeutic possibilities of plasmonically heated gold nanoparticles," *TRENDS in Biotechnology*, vol. 24, no. 2, pp. 62–67, 2006.

[2] I. El-Sayed, X. Huang, and M. El-Sayed, "Selective laser photo-thermal therapy of epithelial carcinoma using anti-egfr antibody conjugated gold nanoparticles," *Cancer letters*, Jan 2006.

[3] L. Paasonen, T. Laaksonen, C. Johans, M. Yliperttula, K. Kontturi, and A. Urtti, "Gold nanoparticles enable selective light-induced contents release from liposomes," *Journal of Controlled Release*, vol. 122, no. 1, pp. 86–93, 2007.

[4] E. Connor, J. Mwamuka, A. Gole, and C. Murphy, "Gold nanoparticles are taken up by human cells but do not cause acute cytotoxicity," *Small*, Jan 2005.

[5] T. Numata, H. Tatsuta, Y. Morita, Y. Otani, and N. Umeda, "Localized thermal processing with a laser-trapped and heated metal nanoparticle," *IEEJ Transactions on Electrical and Electronic Engineering*, vol. 2, no. 3, 2007.

[6] J. A. Stratton, "Electromagnetic theory," 1941.

[7] C. F. Bohren and D. R. Huffman, "Absorption and scattering of light by small particles," *Wiley*, 1983.

[8] U. Kreibig, "Optical properties of metal clusters," *Springer*, 1995.

[9] U. Kreibig, "Hundert jahre mie-theorie. optische eigenschaften von nanopartikeln," *Physik in unserer Zeit*, Jan 2008.

[10] W. Wiscombe, "Improved mie scattering algorithms," *Applied Optics*, Jan 1980.

[11] G. Mie, "Beiträge zur optik trüber medien, speziell kolloidaler metallösungen," *Ann. Phys*, vol. 25, no. 3, pp. 377–445, 1908.

[12] G. Hale and M. Querry, "Optical constants of water in the 200-nm to 200-m wavelength region," *Applied Optics*, vol. 12, no. 3, pp. 555–563, 1973.

[13] P. Johnson and R. Christy, "Optical constants of the noble metals," *Physical Review B*, Jan 1972.

[14] T. Klar, M. Perner, S. Grosse, and G. V. Plessen, "Surface-plasmon resonances in single metallic nanoparticles," *Physical review letters*, Jan 1998.

[15] S. Link and M. El-Sayed, "Size and temperature dependence of the plasmon absorption of colloidal gold nanoparticles," *Journal of Physical Chemistry B*, Jan 1999.

[16] *http://nanopartz.com/Nanopartz%20images/Nanoparticles%20and%20sizes%20and%20distribution.jpg*.

[17] *http://www.webexhibits.org/causesofcolor/9.html*.

[18] A. Ashkin, "Acceleration and trapping of particles by radiation pressure," *Physical review letters*, Jan 1970.

[19] A. Ashkin, J. Dziedzic, J. Bjorkholm, and S. Chu, "Observation of a single-beam gradient force optical trap for dielectric particles," *Optics letters*, Jan 1986.

[20] A. Ashkin, "Forces of a single-beam gradient laser trap on a dielectric sphere in the ray optics regime1," *Methods in cell biology*, vol. 55, pp. 1–27, 1997.

[21] G. Roosen and C. Imbert, "Optical levitation by means of two horizontal laser beams: a theoretical and experimental study," *Physics Letters A*, Jan 1976.

[22] K. Svoboda and S. Block, "Optical trapping of metallic rayleigh particles," *Optics letters*, Jan 1994.

[23] W. Doyle, "Optical properties of a suspension of metal spheres," *Physical Review B*, Jan 1989.

[24] P. Hansen, V. Bhatia, N. Harrit, and L. Oddershede, "Expanding the optical trapping range of gold nanoparticles," *Nano Letters*, vol. 5, no. 10, pp. 1937–1942, 2005.

[25] K. Neuman and S. Block, "Optical trapping," *Review of Scientific Instruments*, Jan 2004.

[26] D. Boal, "Mechanics of the cell," *Cambridge University Press*, 2002.

[27] P. Hansen, I. Tolic-Nørrelykke, and H. Flyvbjerg, "tweezercalib 2.1: Faster version of matlab package for precise calibration of optical tweezers," *Computer Physics ...*, Jan 2006.

[28] J. Nagle and H. S. Jr, "Lateral compressibility of lipid mono-and bilayers. theory of membrane permeability," *Biochimica et Biophysica Acta (BBA)- ...*, Jan 1978.

[29] T. Heimburg, "Mechanical aspects of membrane thermodynamics. estimation of the mechanical properties of lipid membranes close to the chain melting transition from calorimetry," *Biochimica et Biophysica Acta (BBA)-Biomembranes*, Jan 1998.

[30] A. Blicher, K. Wodzinska, and M. Fidorra, "The temperature dependence of lipid membrane permeability, its quantized nature, and the ...," *Biophysical Journal*, Jan 2009.

[31] P. Bendix, S. Reihani, and L. Oddershede, "... of heating by electromagnetically trapped gold nanoparticles on supported lipid ...," *ACS nano*, 2010.

[32] B. Valeur, "Molecular fluorescence principles and applications," *Wiley*, pp. 1–399, Oct 2002.

[33] A. Rohrbach and E. Stelzer, "Trapping forces, force constants, and potential depths for dielectric spheres in the presence of spherical aberrations," *Applied optics*, Jan 2002.

[34] P. M. Bendix, M. S. Pedersen, and D. Stamou, "Quantification of nano-scale intermembrane contact areas by using fluorescence resonance energy transfer," *PNAS*, pp. 1–6, Jul 2009.

[35] L. Mayer, M. Hope, and P. Cullis, "Vesicles of variable sizes produced by a rapid extrusion procedure," *Biochimica et Biophysica Acta (BBA)- ...*, Jan 1986.

[36] R. Richter, R. Berat, and A. Brisson, "Formation of solid-supported lipid bilayers: an integrated view," *Langmuir*, Jan 2006.

[37] M. Daniel and D. Astruc, "Gold nanoparticles: assembly, supramolecular chemistry, quantum-size-related properties, and applications toward biology, catalysis, and nanotechnology," *Chem. Rev*, vol. 104, no. 1, pp. 293–346, 2004.

[38] P. Hansen, "Cellular mechanics studied by novel nano-tools and reconstituted model systems," *Phd. Thesis*, 2007.

[39] D. Needham and E. Evans, "Structure and mechanical properties of giant lipid (dmpc) vesicle bilayers from 20. ...," *Biochemistry*, Jan 1988.

[40] S. Pedersen, K. Jørgensen, T. Baekmark, and O. Mouritsen, "Indirect evidence for lipid-domain formation in the transition region of phospholipid bilayers by two-probe fluorescence energy transfer," *Biophysical Journal*, vol. 71, no. 2, pp. 554–560, 1996.

[41] N. S. Reihani 2007.

[42] H. Goldenberg and C. Tranter, "Heat flow in an infinite medium heated by a sphere," *British Journal of Applied Physics*, vol. 3, pp. 296–298, 1952.

[43] S. Block, "Optical tweezers: a new tool for biophysics," *Modern cell biology*, Jan 1990.

[44] A. Schönle and S. Hell, "Heating by absorption in the focus of an objective lens," *Optics letters*, Jan 1998.

[45] Y. Liu, G. Sonek, M. Berns, and B. Tromberg, "Physiological monitoring of optically trapped cells: assessing the effects of confinement by 1064-nm laser tweezers using microfluorometry," *Biophysical Journal*, Jan 1996.

[46] E. Peterman, F. Gittes, and C. Schmidt, "Laser-induced heating in optical traps," *Biophysical Journal*, Jan 2003.

[47] Y. Seol, A. Carpenter, and T. Perkins, "Gold nanoparticles: enhanced optical trapping and sensitivity coupled with ...," *Optics letters*, Jan 2006.

[48] A. Urban, M. Fedoruk, M. Horton, and J. O. Rädler, "Controlled nanometric phase transitions of phospholipid membranes by plasmonic heating of single gold nanoparticles," *Nano Letters*, 2009.

[49] V. Kotaidis, C. Dahmen, F. Springer, A. Plech, and G. von Plessen, "Excitation of nanoscale vapor bubbles at the surface of gold nanoparticles in water," *THE JOURNAL OF CHEMICAL PHYSICS*, pp. 1–7, May 2006.

[50] R. Saija, P. Denti, F. Borghese, and O. Maragò, "Optical trapping calculations for metal nanoparticles. comparison with experimental data ...," *Optics Express*, Jan 2009.

[51] H. Kurita, A. Takami, and S. Koda, "Size reduction of gold particles in aqueous solution by pulsed laser irradiation," *Applied Physics Letters*, Jan 1998.

[52] A. Govorov and H. Richardson, "Generating heat with metal nanoparticles," *Nano Today*, vol. 2, no. 1, pp. 30–38, 2007.

[53] A. Skirtach, A. M. Javier, O. Kreft, K. Kohler, A. P. Alberola, H. Mohwald, W. Parak, and G. Sukhorukov, "Laser-induced release of encapsulated materials inside living cells," *Angewandte Chemie*, vol. 118, no. 28, 2006.